Journal Pre-proof

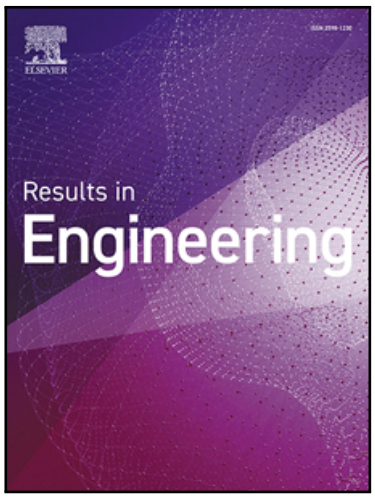

Electrochemical Behavior of Biochar, Molybdenum Trioxide and Graphene Nanocomposite for Supercapacitors

Mehran Saeed , Shumaila Karamat , Ahmed.N.M. Alahmadi , Mohammed Aman , Irfan Sabir , Muhammad Kashif , Muhammad I. Masud , Farid Ullah

PII: S2590-1230(25)04148-9
DOI: https://doi.org/10.1016/j.rineng.2025.108102
Reference: RINENG 108102

To appear in: *Results in Engineering*

Received date: 3 August 2025
Revised date: 21 October 2025
Accepted date: 5 November 2025

Please cite this article as: Mehran Saeed , Shumaila Karamat , Ahmed.N.M. Alahmadi , Mohammed Aman , Irfan Sabir , Muhammad Kashif , Muhammad I. Masud , Farid Ullah , Electrochemical Behavior of Biochar, Molybdenum Trioxide and Graphene Nanocomposite for Supercapacitors, *Results in Engineering* (2025), doi: https://doi.org/10.1016/j.rineng.2025.108102

This is a PDF of an article that has undergone enhancements after acceptance, such as the addition of a cover page and metadata, and formatting for readability. This version will undergo additional copyediting, typesetting and review before it is published in its final form. As such, this version is no longer the Accepted Manuscript, but it is not yet the definitive Version of Record; we are providing this early version to give early visibility of the article. Please note that Elsevier's sharing policy for the Published Journal Article applies to this version, see: https://www.elsevier.com/about/policies-and-standards/sharing#4-published-journal-article. Please also note that, during the production process, errors may be discovered which could affect the content, and all legal disclaimers that apply to the journal pertain.

© 2025 Published by Elsevier B.V.
This is an open access article under the CC BY-NC-ND license (http://creativecommons.org/licenses/by-nc-nd/4.0/)

Highlights

- Synthesized MoO_3/MLG/biochar (MGB 2) composites using hydrothermal technique.
- MLG improves the conductivity and provide structural support to redox-active MoO_3.
- The porous biochar increases the surface area and lowers overall composite cost.
- MGB 2 composite showed highest Csp of 367.8 F g^{-1} at 1 mVs^{-1} in the CV analysis.
- In GCD analysis, MGB 2 exhibited the highest Csp of 385 F g^{-1} at 1 A g^{-1}.
- MGB 2 delivered 16.17 Wh kg^{-1} energy density at 1 A g^{-1}.

Journal Pre-proof

Electrochemical Behavior of Biochar, Molybdenum Trioxide and Graphene Nanocomposite for Supercapacitors

Graphical Abstract

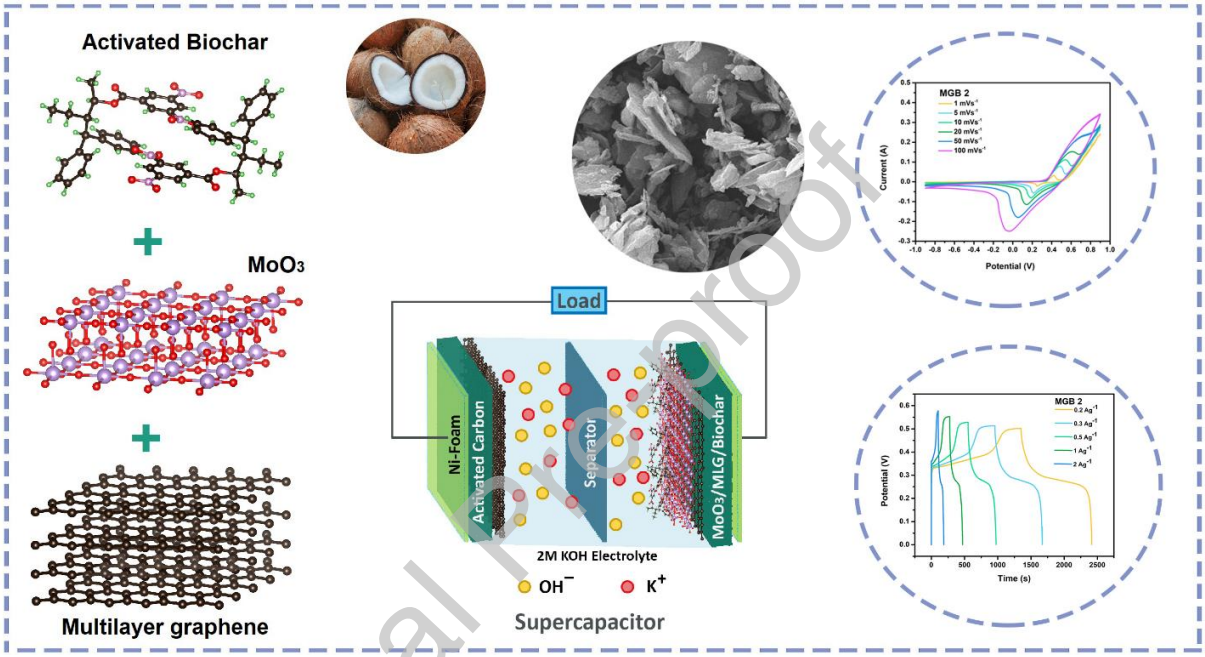

Journal Pre-proof

Journal Pre-proof

Electrochemical Behavior of Biochar, Molybdenum Trioxide and Graphene Nanocomposite for Supercapacitors

[1]*Mehran Saeed,* [1]*Shumaila Karamat,* [2]*Ahmed. N. M. Alahmadi,*[3]*Mohammed Aman,* [4]*Irfan Sabir,* [5]*Muhammad Kashif,*[6]*Muhammad I. Masud,* [1]*Farid Ullah*

[1]*Electrochemical Materials and Devices Laboratory, Department of Physics, COMSATS University Islamabad 45550, Pakistan*

[2]*Department of Electrical Engineering, Umm Al-Qura University, Makkah 21955, Saudi Arabia.*

[3]*Department of Industrial Engineering, College of Engineering, University of Business and Technology, Jeddah, 21361, Saudi Arabia.*

[4]*School of Precision Instrument and Optoelectronics Engineering, Tianjin University, 92 Weijin Road, Nankai District, Tianjin 300072, China*

[5]*School of Electrical and Information Engineering, Tianjin University 92 Weijin Road, Nankai District, Tianjin 300072, China*

[6]*Department of Electrical Engineering, College of Engineering, University of Business and Technology, Jeddah 21361, Saudi Arabia*

Corresponding author: Dr. Shumaila Karamat

E-mail address: shumailakaramat@comsats.edu.pk, shumailakaramat@gmail.com

Journal Pre-proof

Abstract

In this research study, we report the preparation of coconut husk-based nanocomposites containing molybdenum trioxide (MoO_3), and multilayer graphene (MLG), using a one-pot hydrothermal technique. The ternary composite, having an optimized composition of MoO_3, MLG, and biochar (80:10:10), exhibited a layered and porous morphology with MoO_3 nanoparticles homogenously distributed inside the layered graphene and biochar matrix. XRD analysis confirmed the formation of orthorhombic MoO_3 nanoparticles and a carbonaceous framework. The composite material was characterized by FTIR and XPS to verify its composition and chemical states. BET study further confirmed the porous surface of the nanocomposite due to the addition of coconut husk-based biochar. Surface morphology was

Journal Pre-proof

analyzed using FESEM, and EDX results indicated the presence of Mo, O, and C in the material. Electrochemical characterization revealed a specific capacitance (C_{SP}) of 385.06 F g^{-1} at 1 A g^{-1} for the above-mentioned composite labeled as MGB 2. Moreover, CV analysis demonstrated a diffusion-type charge storage behavior of MGB 2 composite with improved rate capability, which is associated with the synergistic interaction of pseudocapacitive MoO_3 with highly conductive MLG and porous biochar. The prepared asymmetric supercapacitor device exhibited an energy density of 46.65 Wh kg^{-1} with a power density of 795 W kg^{-1} at 1 A g^{-1}. The device delivered 91.27% of capacitance retention after 7000 cycles. This research sheds light on the potential of using low-cost biomass-based biochar, graphene, and MoO_3 for a scalable and high-performance electrode material for supercapacitor applications.

Keywords: Biochar, MoO_3, multilayer graphene, hydrothermal method, supercapacitors

1. Introduction

Now a days, the research community around the world is focusing on renewable energy resources that do not cause pollution and support zero-carbon emission, such as wind, hydropower, solar, and biomass energy. This search for zero-carbon emission energy sources has boosted the research for high performance energy storage systems. Among these systems, batteries and supercapacitors (SCs) are the most pivotal devices to store energy, especially for electric vehicles and other transport applications. SCs are gaining great interest of researchers for high-power applications, because they can deliver quick burst of energy which make them particularly effective for regenerative braking systems in electric vehicles and other devices that require instantaneous high-power output. This property of SCs improves the fuel efficiency in transportation systems while eliminating carbon emissions in the atmosphere. However, their commercial application is limited due to low energy density, particularly for those applications that require longer energy support. As a result, research efforts are now concentrated on overcoming this challenge, particularly through the design of novel materials that demonstrate high specific capacitance, superior conductivity, and robust structural integrity [1,2].

Two-dimensional (2D) metal oxides have emerged as a key focus in supercapacitor research, primarily due to their ability to exhibit pseudo-capacitance. Transition metal oxides with layered nanostructures are particularly promising, as their high surface atom exposure enables efficient

electron transfer and rapid faradaic processes. Molybdenum trioxide, a notable example, exhibits several advantageous characteristics, including excellent charge transport properties, intrinsic semiconducting behavior, and a unique interlayer structure that can host multiple cations. With a theoretical specific capacity reaching approximately 1005 C/g [3], MoO_3 demonstrates considerable potential as a suitable material for high-performance power storage devices, especially for SCs. However, MoO_3 has few drawbacks that limit its practical application, including its low electrical conductivity (~ 3.78×10^{-5} Scm^{-1} at RT) and sluggish reaction kinetics. These challenges reduce the overall electrochemical performance of MoO_3. To alleviate these limitations, one of the most effective strategies is to combine MoO_3 with highly conductive material to form a composite structure. Carbonaceous materials, including graphene, CNTs, carbon-nanofibers, and graphene oxide (GO),are proven to be the most suitable candidates for this purpose [4].

Recently, the research on hybrid materials for supercapacitor application, especially combining pseudocapacitive material like TMOs with highly conductive carbon-based materials has gained significant attention among the research community [5-6]. This approach synergizes the reversible faradic charge storage and electrostatic charge storage approaches to boost the overall electrochemical characteristics of the electrode material [7]. Many research papers have reported enhanced electrochemical performance of MoO_3/carbon-based nanocomposites. A MoO_3-rGO composite was synthesized using a microwave-assisted approach, delivering a CSP of 133.68 Fg^{-1}, with an Ed of 36.2 $Whkg^{-1}$ and a P_d of 535.6 Wkg^{-1}. It also showed enhanced cycling performance, maintaining 85% of its initial C_{SP}after 4000 cycles [8]. In another report, MoO_3-rGO nanohybrid was synthesized using hydrothermal approach which achieved a significantly high capacity of 607.82 Cg^{-1}. An asymmetric device based on MoO_3-rGO//rGO was also fabricated, which delivered a specific capacity of 188.40 Cg^{-1}, with E_d of 36.78 $Whkg^{-1}$ and P_d of 2546.84 Wkg^{-1}. The cell delivered 87.6% of capacity retention over 10000 cycles [9]. A CNT/MoO_3 nanocomposite was also reported which achieved a C_{SP} of 274 Fg^{-1} at 2 mV s^{-1} [10]. In another report, MoO_3@CNTs nanocomposite showed an exceptionally high C_{SP} of 1165.4 Fg^{-1} at 1 mAg^{-1}[11]. The above-mentioned figures show the importance of carbonaceous material in optimizing the EC properties of MoO_3-based composites.

Carbonaceous materials includingGraphene, reduced graphene oxide (rGO), CNTs, and carbon-nanofibers have been explored for diverse applicationssuch as energy storage, photocatalysis, and sensing [12-13]. These materials have shown excellent electrochemical properties when they are used as a SC+ electrode material. Biomass-derived carbon-based materials such as biochar have attracted the interest of researchersdue to its multiple advantages including, cost-effective synthesis, tunable physical and chemical properties and environment friendly nature [14]. When biochar is integrated with other carbonaceous materials like CNTs and graphene, it not only reduces the overall cost of the material but its porous structure also enhances ion diffusion in the composite material [15].In a recent study, cobalt nanofibers and orange peel-derived biochar (CoNF@OBC) nanocomposite was synthesized using solvothermal route, which has showed a notable C_{SP} of 563 Fg^{-1} at1 Ag^{-1} [16]. In another research publication, nitrogen and boron doped biochar with porous surface was synthesizedby the carbonization of cellulose aerogel, which demonstratedC_{SP} of 220.9 Fg^{-1} [17].Recently, rice husk-derived biochar, MoO_3 and NiO_2 ternary composite were prepared using solid-state pyrolysis. The synthesized C-MoO_3-NiO_2 nanocomposite has delivered C_{SP} of 180.77 F g^{-1} at 1 A g^{-1} with 75% retentionafter 1000 cycles [66]. In another study, carbon-coated MoO_3 and rGO nanocomposites were synthesized using a hydrothermal technique. The composite delivered 562 F g^{-1} at 1 A g^{-1}, the composite also showed excellent cyclic performance [71].Despite these research advancements, the integration of biochar with metal oxides, especially MoO_3 for SCs applications needs further investigation and improvement to unlock their full potential for SC applications.

In this work, binary and ternary nanocomposites were synthesized using a hydrothermal method. These nanocomposites incorporate molybdenum trioxide (MoO_3), multilayer graphene (MLG),and coconut husk based activated biochar.The integration of MoO_3, MLG, and biochar offers a unique set of properties that enhances the overall electrochemical properties of the composite. MoO_3 offers excellent theoretical capacitance due to its multiple redox states and serves as the primary pseudocapacitive material in the composite, but it is limited by poor conductivity and structural degradation during cyclic performance [18]. The incorporation of MLG addresses these issues of MoO_3 by providing enhanced electrical conductivity, an improved surface area, and structural support to prevent agglomeration of MoO_3 nanoparticles [19]. Coconut husk biochar is a low-cost and sustainable carbon material that introduces hierarchical porosity in the composite and promotes efficient ion diffusion [20].The ternary

Journal Pre-proof

composite of MoO_3/MLG/Biochar was synthesized with two different weight ratios of 80:10:10 and 86:7:7. For comparative analysis, binary composites of MoO_3 with activated biochar (MoO_3/Biochar, 80:20) and with multilayer graphene (MoO3/MLG, 80:20) were also synthesized separately.

2. Experimental Details

2.1 Materials Detail

Sodium molybdate dihydrate ($NaMoO_4$. $2H_2O$, 99%), and sodium chloride (NaCl, 99%) were purchased from UNI-Chem. Hydrochloric acid (HCl, 37%) was purchased from SUPELCO, multilayer graphene (99%) was purchased from Sigma-Aldrich, activated biochar (Wood-based Coconut shell Coal-based, 97%) was purchased from China. The reagents were purchased as research grade, and utilizedwithout more purification.

2.2 Synthesis of MoO_3/MLG/biochar

A ternary composite consisting of MoO_3, multilayer graphene, and activated biochar in a weight ratio of 80:10:10 was successfully synthesized using the hydrothermal method [21]. Initially, 1.209 g of $NaMoO_4$. $2H_2O$ (0.1 M) and 0.584 g of NaCl (0.2 M) was put into 30 ml of DI waterand mixedfor half an hour in a glass beaker.NaCl in the precursor solution is used to control the nucleation and growth of MoO_3 during hydrothermal synthesis.To adjust the pH to 2, a few drops of 3 M HCl solution were inserted to the above-mentioned solution and continuously stirred to form a well-dispersed solution.At the same time, 10 wt% multilayer graphene and 10 wt% activated biochar were each poured in 10 mLDI water in separate beakers and sonicated for 30 minutes to form a uniform dispersion. These two prepared dispersions were then mixed to the primary precursor's solution, and the resulting solution was magnetically stirred continuously for another 60 minutes until a homogenous solution was achieved. The dispersion was inserted into an autoclave and heated at 180 °C for 24 hours in an oven. After removing the autoclave from the oven, the resulting precipitates were rinsed with DI waterusing a centrifuge and dried at 70 °C for 24 hours. The synthesized ternary composite was collected and labeled as MGB 2. For comparison, another ternary sample was synthesized with a reduced quantity of MLG and biochar with a weight ratio of 86:7:7 and labeled as MGB 1. Additionally, two binary

composites, MoO_3/Biochar (80:20) using activated biochar and MoO_3/MLG (80:20) using multilayer graphene, were synthesized for comparative analysis.

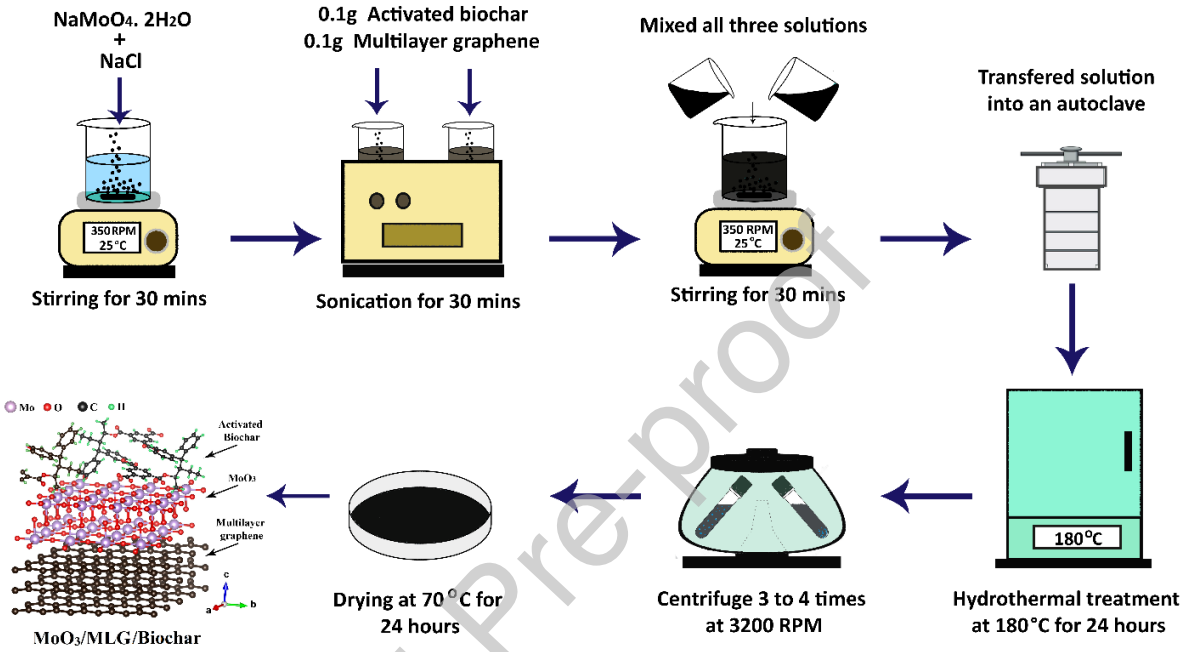

Figure 1: Schematic illustration of hydrothermal preparation of MoO_3/MLG/Biochar composite

3. Experimental Outcomes and Discussion

3.1 XRD Analysis

XRD was employed to study the crystalline architecture of the prepared material. Figure 2(a) shows the XRD diffraction pattern of MGB 2. All diffraction peaks in the spectrum can be identified as orthorhombic MoO_3, which was confirmed from the reported pattern [JCPDS no. 00-05-0508].The appearance of intense diffraction peaks situated at 12.74°, 23.31°, 25.63°, 27.28°, 29.7°, 33.84°, 38.96°, 46.35°, 49.22° and 64.98° corresponds to the (020), (110), (040), (021), (130), (111), (060), (210), (002), and (190)crystallographic plans, demonstrated the layered structure of α-MoO_3 [22]. The XRD spectrum also has peaks at 26.49° and 54.5°,which represent MLG [23]. The peaks at 26.49° and 54.5° correspond to (002) and

(004)crystallographic planes,and it is the characteristic peaks of MLG (JCPDS No. 41-1487). Normally, materials with biochar show a broad diffraction hum in the spectra between 20 ° and 25, in case of MGB 2, this hump is not visible.This can be due to the fact that the relative proportion of biochar is low as compared to MoO_3 and the sharp crystalline peaks of MoO_3 overshadow the weaker amorphous hump of biochar.There was no new crystalline phase or impurity found in the XRD spectrum.*To find the crystallite size of MoO_3 within the nanocomposite, the Williamson-Hall (W-H) mathematical approach was used [24]*

$$\beta cos\theta = \frac{k\lambda}{D} + 4\varepsilon\, sin\theta \qquad (1)$$

Where β is the peak broadening at a particular angle θ, D is the crystallite size, k is the wavelength and ε is the lattice-strain. Figure 2(b) shows the linear fitting of the W-H plot (βCosθ vs 4Sinθ). The slope of the plot showed the lattice strain, which was calculated to be 2.2×10^{-3}, and the y-intercept was used to estimate the crystallite size.The estimated crystallite size of *MoO_3 within the composite* was estimated to be 79.13 nm, which was further confirmed using the Scherrer equation.

3.2 FTIR analysis

FTIR study was used to study the specific composition and functional groups in the prepared nanocomposite. A change in the characteristic pattern of absorption bands analyzes the variation in material composition. Figure 2(c) shows the transmittance plot of MGB 2 and MoO_3/biochar nanocomposite. The intense bands between 450 and 900 cm^{-1} are linked with symmetric and asymmetric vibrations of M-O and Mo-O-Mo bonds. The stretching of Mo-O-Mo is visualized at 873 cm^{-1} and the bands associated with the stretching of the Mo-O bondare identified at 481 and 620.7 cm^{-1} [25-26]. The band appearing at 995.8 cm^{-1} is due to the stretching of M=O bond [27]. Furthermore, the peaks at 1122.4, 1384.8, and 1617.4 $cm^{-1}$are linked with C-O, C-C, and C=C bond vibrations [28]. The depressed peaks appeared at 2031.7 and 2366 cm^{-1} are due to stretching of C-O and C-H bonds [29]. The broad absorption centered around 3414.3 cm^{-1} indicates hydrogen-bonded O–H groups or adsorbed moisture [30]. By comparing the FTIR spectra of MoO_3/biochar and MGB 2 composite, the percentage of transmittance is significantly reduced by the addition of multilayer graphene. This reduction of peaks in MGB 2 can be

attributed to the integration of MLG, which significantly changes the optical response of the material [31]. FTIR analysis indicates the successful integration of MoO_3 with the carbon matrix of MLG and biochar.

3.3 Raman Spectroscopy

The Raman spectra of the MGB 2 and MoO_3/MLG composite in the spectral window of 0–3000 cm^{-1} are presented in Figure 2(d). The graph contains the characteristic vibrational features of orthorhombic phase of MoO_3, and carbonaceous contents. In the lower-wave number range, the intense peak at 986 $cm^{-1}$is due to the non-symmetric vibration of the Mo=O terminal bond. The signal appeared at 814 $cm^{-1}$and 660 cm^{-1} arerelated to asymmetric stretching, an intense signal at 814 cm^{-1} originates by corner-sharing and peak at 660 cm^{-1} is originated by edge-sharing Mo_2-Obonds in the octahedral lattice [32].The band with low intensity at 466 cm^{-1} is formed because ofthe vibrational mode of O-Mo-O bonds, and it is associated with the stretching of A_g mode [33]. The signal at 270 cm^{-1} is linked to the twisting of the O=Mo=O bond (B_{2g}, B_{3g}) [34]. The intense signal at 127 cm^{-1} is because of the translational $[MoO_4]_n$ rigid chain modes [35]. The peaks observed in the spectra confirm the successful synthesis of MoO_3. In the high-wavenumber region, a prominent D band (1350 cm^{-1}) and a G band (1580 cm^{-1}) are visible in the spectra, indicating sp^2 carbon framework and graphitization degree [36]. The prominent D band shows the structural disorders that can originate due to functional groups or defects in multilayer graphene and activated biochar domains [37]. A broadened 2D band with less intensity as compared to the G band is also observed at 2700 cm^{-1}. The corresponding I_{2D}/I_G ratio is 0.24, which is less than the ratio in monolayer graphene, indicating the incorporation of multilayer graphene in the nanocomposite [38]. Raman spectroscopy of MoO_3/MLG composite was carried out for comparison. The spectrum contains all the prominent peaks of MoO_3, including D and G bands of MLG in the high wavelength region.The Raman spectrum of MGB 2 showed distinct D and G bands at 1350 and 1580 cm^{-1}, respectively, while in the MoO_3/MLG composite, these bands appeared at 1337 and 1567 cm^{-1}. This shift in peak positions and increase in the intensity of D and G bands in MGB 2 as compared to binary composite prove the integration of biochar in the composite. Furthermore, the I_D/I_G ratio for MoO_3/MLG composite was estimated to be 0.26, whereas MGB 2 ternary composite showed a higher I_D/I_G ratio of 0.58. Figure 2(e) shows the comparison of D and G bands for both composites. This increased I_D/I_G ratio of the ternary

composite indicates enhanced structural disorder due to the integration of biochar [39].The presence of well-defined MoO_3 Raman modes between 100 to 1000 cm^{-1} alongside the D, G and 2D carbon bands supports the structural synergy of the composite material.

3.4 BET analysis

To study the porosity characteristics of the composite material, BET measurements were utilized to estimate effective surface area, pore diameter and pore volume. Figure 2(f) shows the isotherm plot for MGB 2. As per the IUPAC hysteresis loop classification, the composite material exhibits type-V isotherm curve with H2(b) hysteresis loop [40]. This indicates the presence of mesopores with ink-bottle-shaped structure in the composite material. This irregular and constricted pore structure can help in ion transport but can also reduce accessible surface area. The open and wide hysteresis loop indicates abundant mesopores with a complex pore network with interconnected mesopores. The MGB 2 nanocomposite demonstrated an effective surface area of 19.11 m^2 g^{-1}, overall pore volume of 0.02302 cm^3 $g^{-1,}$ and apore diameter of 2.53 nm, as calculated by the BJH method. Figure 2(f; inset) presents the pore size distribution of MGB 2. These values confirm the presence of more mesopores with partial contribution from micropores [41]. While the surface area of the composite is comparatively modest, the mesoporous structure ensures efficient ion transport. The pore size distribution and shape of the hysteresis loop suggest that the electrochemical processes in the composite are mainly governed by pore accessibility and diffusion pathways.

Journal Pre-proof

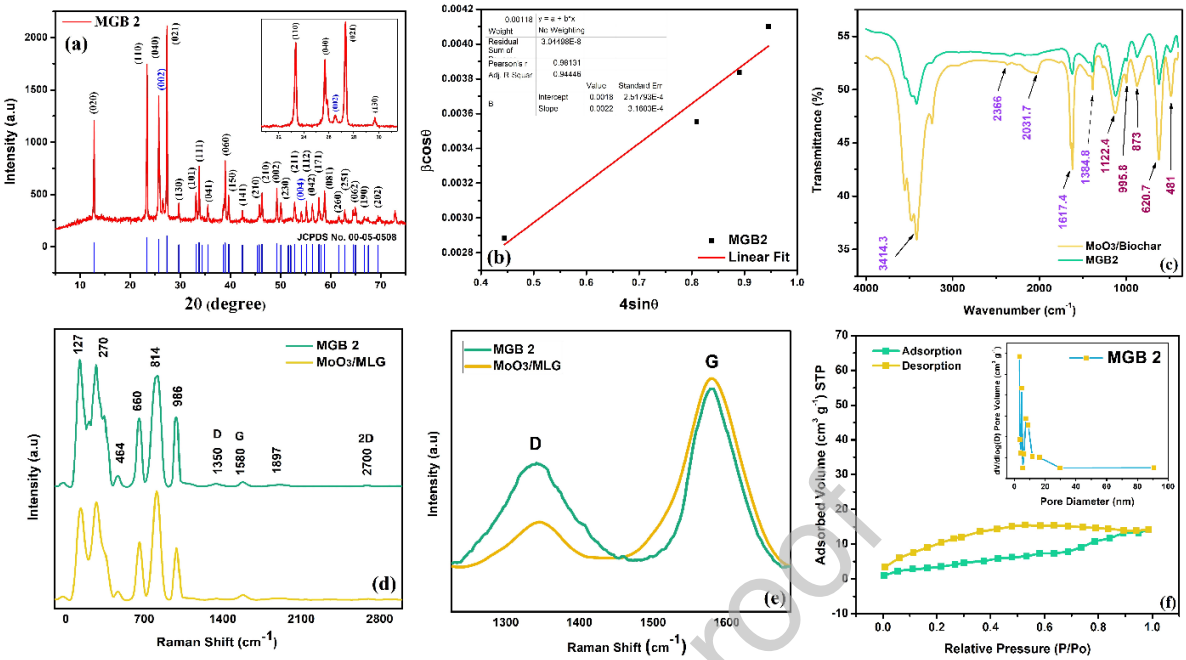

Figure 2: (a) XRD spectra of MGB 2, (b) Williamson-Hall Plot of MGB 2, (c) FTIR spectra of MGB 2 and MoO_3/biochar nanocomposite, (d) Raman spectra of MGB 2 and MoO_3/MLG, (e) Raman spectra showing the comparison of D and G bands of MGB 2 and MoO_3/MLG, (f) BET isotherm of MGB 2 (pore size distribution plot of MGB 2 in shown in inset)

3.5 XPS analysis

XPS analysis was carried out using ESCALAB Xi+ instrument (Thermo SCIENTIFIC) to study the composition and electronic states of MGB 2 nanocomposite. The deconvoluted peaks from the XPS spectrum were interpreted using the NIST XPS database. The main survey scan of the composite is shown in Figure 3(a), which displays distinct peaks corresponding to Mo3d, Mo3p, Mo4s, Mo3s, C1s, and O1s, showing the presence of required elements in the prepared composite material. The atomic percentage of the composite was estimated as Mo (31.09%), O (23.11%) and C (45.8%). The deviation between the nominal and XPS-determined atomic composition can be due to the surface-sensitive nature of XPS. The presence of multilayer graphene and biochar on the surface can increase the carbon signal. Such discrepancies are expected in heterogeneous composites [88]. The XPS spectrum also displayed additional peaks associated to the 4p, 3p and 3s subshells of Mo atoms. The signals at 40.9 eV, 399.4 eV, 416.5 eV, and 510.9 eV correspond to 4p3/2, 3p3/2, 3p1/2, and 3s orbitals of Mo, respectively [42–44].

The Mo 3d peak is analyzed in detail by high-resolution XPS, displayed in Figure3(b). The spectrum exhibited dominant deconvoluted peaks at 232.8 eV, 236.0 eV, and 237.5 eV, which is associated with the Mo3d5/2 and Mo3d3/2 doublets, demonstrating Mo in +6 oxidation state confirms the Mo-O bonding [45-47]. In figure 3(c), the O1s resolution scan exhibits the intense peak at 530.6 eV, followed by a low-intense peak at 531.6 eV. An intense O1s peak at 530.6 eV is associated with the Mo-O bond, which originates from lattice oxygen in MoO_3, and the low-intense peak at 531.6 eV is associated to residual oxygen bonded to carbon in MLG and biochar [48–49]. Figure 3(d) depicts the resolution scan of C1s with the deconvoluted peaks at 284.3 eV and 285.08 eV. The dominant peak at 284.3 eVis related to the C=C/C-C bonds, and originates from the incorporation of multilayer graphene and biochar in the composite [50]. The low-intense peak at 285.08 eV presents the C-O (epoxy) bond, which is normally observed in the graphene-related composites [51]. These findings of the XPS survey scan of MGB 2 demonstrate the successful integration of MLG and porous biochar with MoO_3 nanoparticles.

Journal Pre-proof

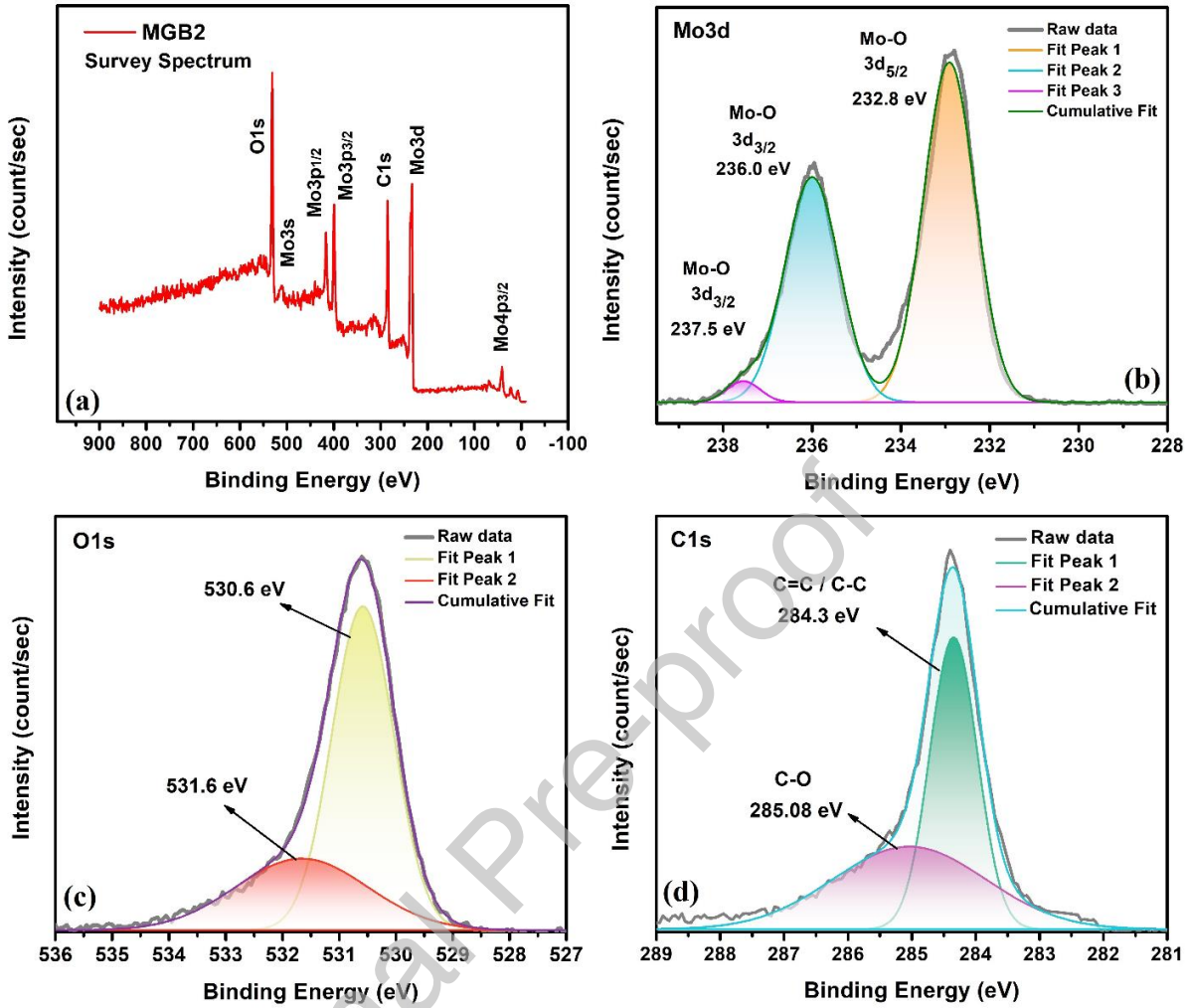

Figure:3(a) XPS survey scan of MGB 2, high-resolution scan of (b) Mo3d, (c) O1s, and (d) C1s

3.6 SEM and EDX analysis

The SEM micrographs were utilized to investigate the surface morphology of MGB2 nanocomposite. Figure 4(a-b) depicts the magnified images of MGB2 with different magnifications. The SEM micrographs revealed an interconnected morphology with an effective integration between MoO_3, MLG, and activated biochar. The multilayered graphene sheets areevident, having a wrinkled and crumpled texture that avoids restacking and provides a large surface area for ion intercalation. MoO_3 particles are identified as irregularly shaped clusters that are homogenously embedded within the MLG matrix. The irregular shape with a relatively rough surface indicates the successful anchoring of nanoparticles on MLG with strong interfacial

interaction with graphene sheets [52]. The biochar is visible as a disordered carbonaceous framework, which further enhances the properties of the layered graphene matrix. This layered and porous conductive framework facilitates faster ion transportation, essential for high electrochemical performance [53]. Furthermore, the homogenous dispersion of MoO_3 nanoparticles within the MLG-biochar conductive network forms a continuous electron-ion pathway with abundant electroactive sites for enhanced charge storage [54]. The SEM images confirm the formation of MoO_3/graphene/biochar ternary composite with enhanced electrochemical properties. The elemental characterization of MGB 2 was carried out by using EDX measurements. Figure 4(c-f) shows the elemental mapping of MGB 2, C, O, and Mo, respectively. The mapping verifies the existence of Mo, O, and C in the composite. The detection of Mo, O, and C in the composite via elemental mapping, together with XRD, Raman, and XPS results, confirms the successful integration of MoO_3, MLG, and biochar in the composite.

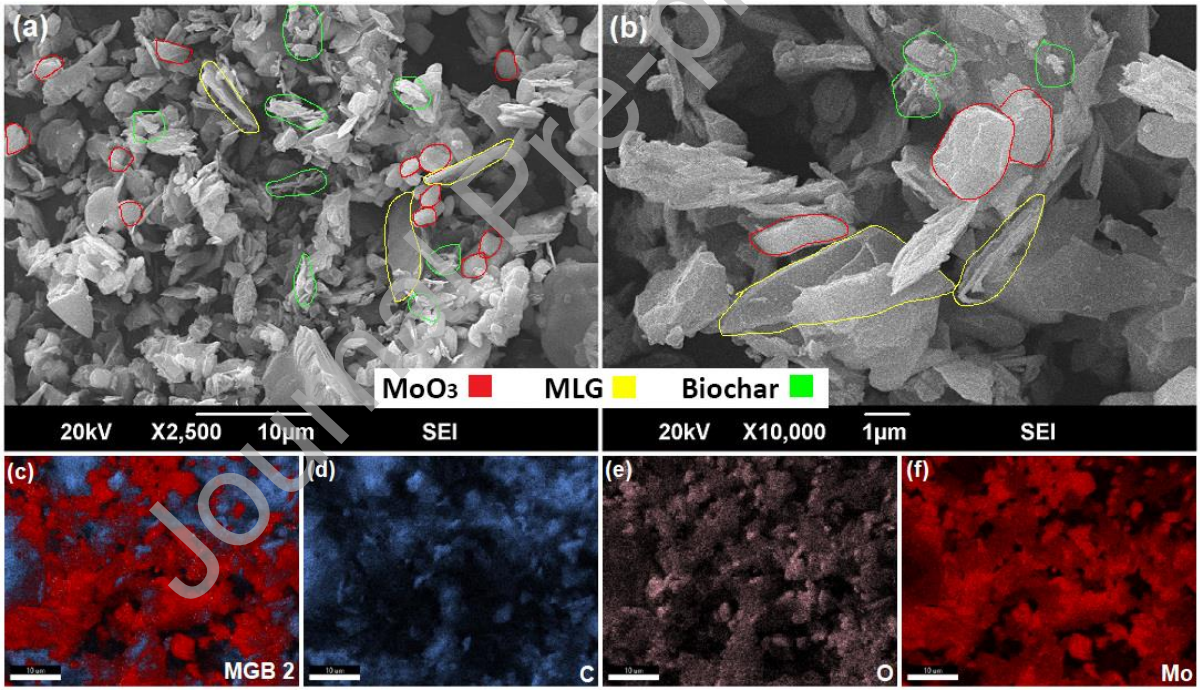

Figure 4: (a) SEM micrographof MGB 2 at 10µm, (b) SEM micrograph of MGB 2 at 1µm, (c) EDX elemental mapping of MGB 2, (d) C, (e) O, (f) Mo

3.7 TEM analysis

The microstructure of MGB 2 was further investigated by TEM analysis. Figure 5(a) and 5(b) depict TEM images of MBG 2 at 200nm and 10 nm respectively. The micrographs reveal a heterogenous structure containing overlapped and wrinkled nanosheets, which can be attributed to MLG. The darker contrast regions are attributed to MoO_3 nanoparticles. HRTEM images confirm the crystalline nature of these particles, showing well-defined lattice fringes with interplanar spacing of 0.22 nm and 0.32 nm, corresponding to the d-spacing of (110) and (021) plans of orthorhombic MoO_3 [55]. TEM micrographs also displayed an amorphous region with diffuse contrast, indicating the activated biochar in the composite. The intimate contact between MoO_3 nanoparticles and carbon matrix of MLG and biochar is visible in several regions, where lattice fringes extend up to the carbon domain, indicating strong interfacial interaction [56]. Furthermore, the nanoscale dimensions and dispersion of MoO_3 nanoparticles within the carbon matrix are in good agreement with the XRD and SEM analysis, which further support the successful integration of crystalline MoO_3, graphitic domains and amorphous biochar**.**

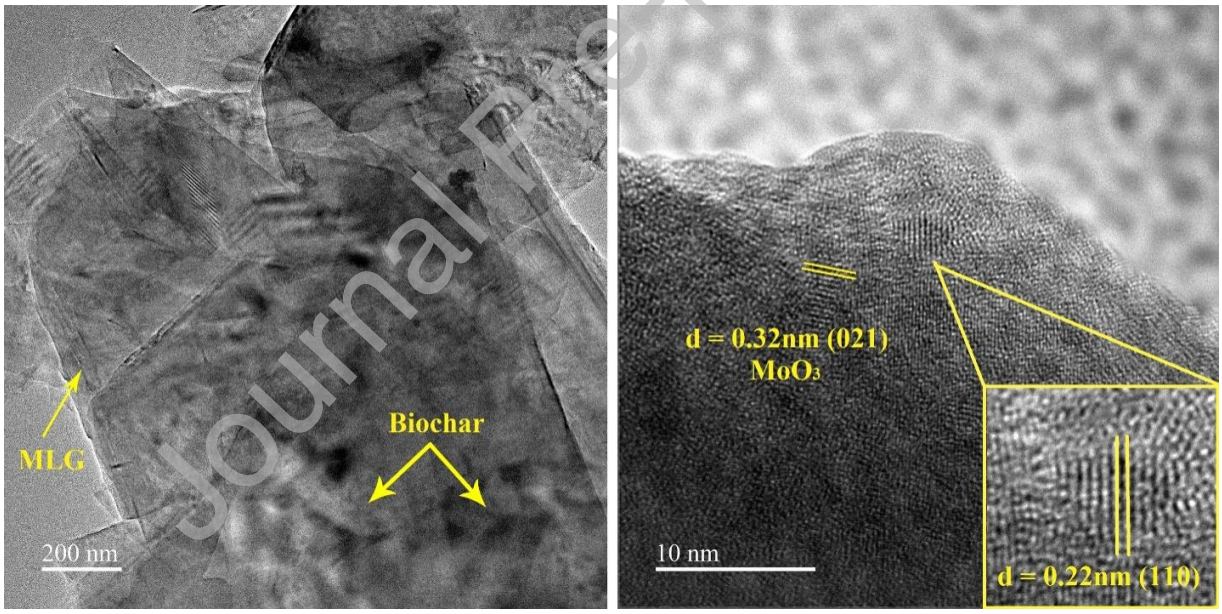

Figure 5: (a) TEM image of MGB 2, (b) HR-TEM image of MGB 2

3.4 The Cyclic voltammetry (CV)

The CV measurements were employed to study the electrochemical (EC) response of the synthesized composites. The measurements are obtained in 1 M KOH electrolytic solution between the optimum potential range of −0.8 to +0.8 V by using a three-electrode electrochemical workstation. This voltage window is selected as it gives maximum area under the curve, and distinct redox peaks during the CV measurements. Figures 6(a), 6(b), 6(c), 6(d), 6(e), 6(f), and 6(g) show the CV curves of MGB 2, MGB 1, MoO_3/biochar, MoO_3/MLG, MoO_3, biochar, and MLG electrodes, respectively, recorded at various sweep-rates between 1 to 100 mV s^{-1}. Unique redox peaks are appeared in each CV profile, which acknowledges the presence of pseudocapacitive behavior and battery-type characteristics in the electrode material [57]. The geometry of CV curves remained unchanged at various sweep rates, which is due to the enhanced conductivity and well-developed porous surface of the electrode material [58]. The oxidation peak is clearly shifted in the direction of positive voltage, while the reduction peak is displaced towards the opposite direction, resulting in increased separation between these peaks, which can be due to the electrode polarization and high interfacial charge transfer resistance at high scan rate [59]. Figure 6(h) depicts the comparative view of CV profiles of all samples at 10 mV s^{-1}. The CV integral area of MGB 2 is higher as compared to MGB 1 and other electrode materials, which shows it higher electrochemical performance. The C_{SP} of all prepared electrodes is estimated from the CV graphs by the following formula,

$$Csp = \frac{\int I.dV}{m.S.\triangle V} \qquad (2)$$

The C_{SP} of MoO_3/MLG, MoO_3/biochar, MGB1 and MGB2 are calculated to be 133.5,206.4, 248.7, and 367.8 Fg^{-1} at 1 mVs^{-1} sweep-rate respectively. The C_{SP} for the MoO_3, biochar, and MLG are calculated to be 122.9, 95.9, and 84.6 at 1 mVs^{-1} scan-rate respectively. MGB 2 is found to exhibit higher value of C_{SP} as compared to the other materials. Figure 6(i) shows the relationship of C_{SP} and scan rate for all synthesized composites. From the CV spectra, it is clear that the shape of the curves is not changed significantly with rise in the scan rate, which demonstrates excellent electrochemical properties of the nanocomposite [60]. These results can be due to the synergic effect of MoO_3, MLG and biochar. Furthermore, power law was used to understand the behavior of MGB 2 nanocomposite. Table 1, summarizes the C_{SP} for all the samples based on CV analysis. Figure 7(a) illustrates the logarithmic plot of current vs scan rate

in both anodic and cathodic scan at 0.4V. This analysis helped us to differentiate between the surface-type and diffusion-type mechanisms of the electrode material [61].

$$\boldsymbol{I_{peak} = a\, v^{b}} \quad (3)$$

$$\boldsymbol{log(I_{peak}) = b\, log(v) + log(a)} \quad (4)$$

In these above equations, I represent applied current, *v*is the sweep-rate used during measurements, a and b represent the variables. The slope of the fitted log(I_{peak}) vs log(v) graph represents the bvalue. If the value of b is 0.5, it showsa dominant diffusion-type charge storage, if b is close to 1, it shows a dominant capacitivecharge storage behavior, and if b value is between 0.5 and 1, it represents amixed behavior of the electrode material [62]. The b-value for MGB 2 was calculated using the slope of the fitted logarithmic plot of current vs scan rate in both anodic and cathodic scan at multiple potentials. The estimated b-value for anodic curves was between 0.4 and 0.7 and for cathodic curve it was estimated between -0.7 and 0.4, demonstrating a dominant diffusion-type charge storage behavior of the material. Figure 7(a) represents b-values for anodic and cathodic curves at 0.4V potential.

Journal Pre-proof

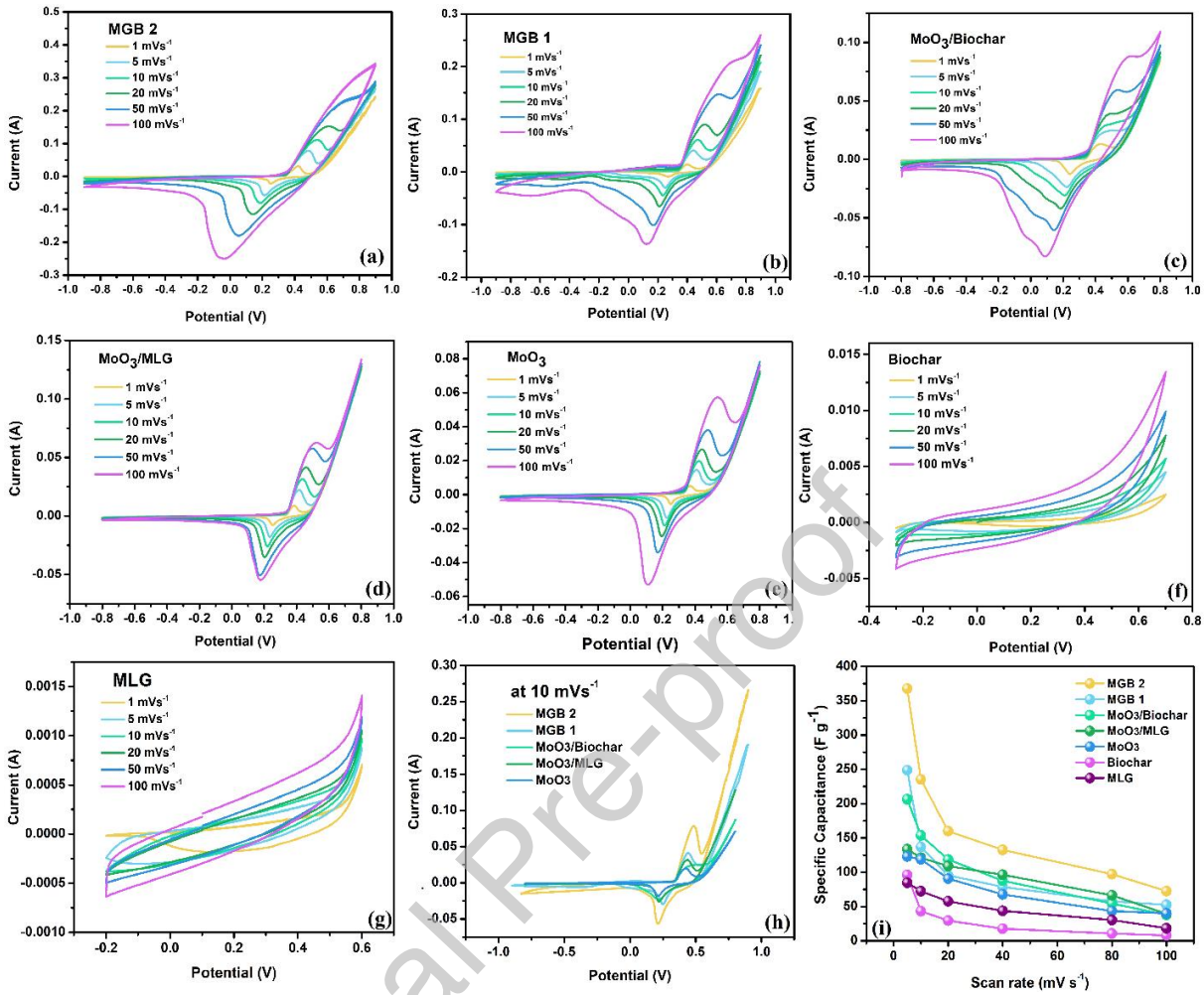

Figure 6: (a) CV profiles of MGB 2at multiplesweep rates, (b) CV profilesofMGB 1, (c) CV profilesofMoO_3/Biochar, (d) CV profiles of MoO_3/MLG, (e) CV profiles of MoO_3, (f) CV profiles of Biochar,(g) CV profiles of MLG, (h) comparative view of CV curves of all samplesat 10 mVs^{-1} sweep rate, (i) C_{SP} vs sweep-rate graph of all samples

Dunn method was utilized to identify the diffusion-type and capacitive-type charge storage behavior of the MGB 2.Figure 7(b) shows the diffusion-control analysis Plot for MGB 2, linear-fit of $I(peak)\ vs\ \sqrt{\boldsymbol{v}}$ plot yielded high correlation coefficient (R^2 = 0.9529 for anodic and 0.9706 for cathodic peaks), this good linear fit suggests that the electrode material follows diffusion-controlled kinetics. The Dunn measurements were performed at different potential for multiple scan rates by the following formula [63].

$$\boldsymbol{I(v) = k_1 v + k_2 \sqrt{v}} \quad (5)$$

Where, $k_1 v$ represents current associated with capacitive-controlled processes and $k_2\sqrt{v}$ represents current due to diffusion-controlled processes. We can rewrite the above equation as follows,

$$\boldsymbol{\frac{I(v)}{\sqrt{v}} = k_1 \sqrt{v} + k_2} \quad (6)$$

Where, k_1 and k_2 values are calculated from the linefitting of $\frac{I(v)}{\sqrt{v}}$ vs $\sqrt{\boldsymbol{v}}$ plot, k_1 is the value of slope of plot and k_2 is estimated from the y-intercept of the fitted curve. Figure 7(c) indicates the Dunn plot of MBG 2, demonstrating the capacitive and diffusion-controlled responses of the material at 10 mVs^{-1}. The measurements were carried out at different potentials for each scan rate. Figure 7(d) depicts the bar graph quantifying the capacitance-type and diffusion-type behavior at differentsweep rates. At 1 mV s^{-1}, the capacitive-type charge storage was estimated to be 15.4%, and the diffusion-controlled charge storage contribution was dominated with 84.6%. As the sweep-rate was elevated, the capacitive contribution was also increased, reaching up to 50.2% at 100 mV s^{-1}, with the diffusion-type charge storage being 49.8 % at 100 mV s^{-1}. This behavior is consistent with typical electrode kinetics, because at lower sweep rates, ions get enough time to penetrate deeper into the bulk and give high dominant diffusion-controlled processes. At an elevated scan rate, ions don't get sufficient time to penetrate into the bulk, which makes capacitive-controlled charge storage more dominant at high scan rates [87]. Importantly, even at a sweep-rate of 100 mVs^{-1}, the diffusion-controlled contribution of the synthesized nanocomposite remains significantly high as compared to many reported systems, which shows highly pseudocapacitive nature of the MGB 2 nanocomposite.

Journal Pre-proof

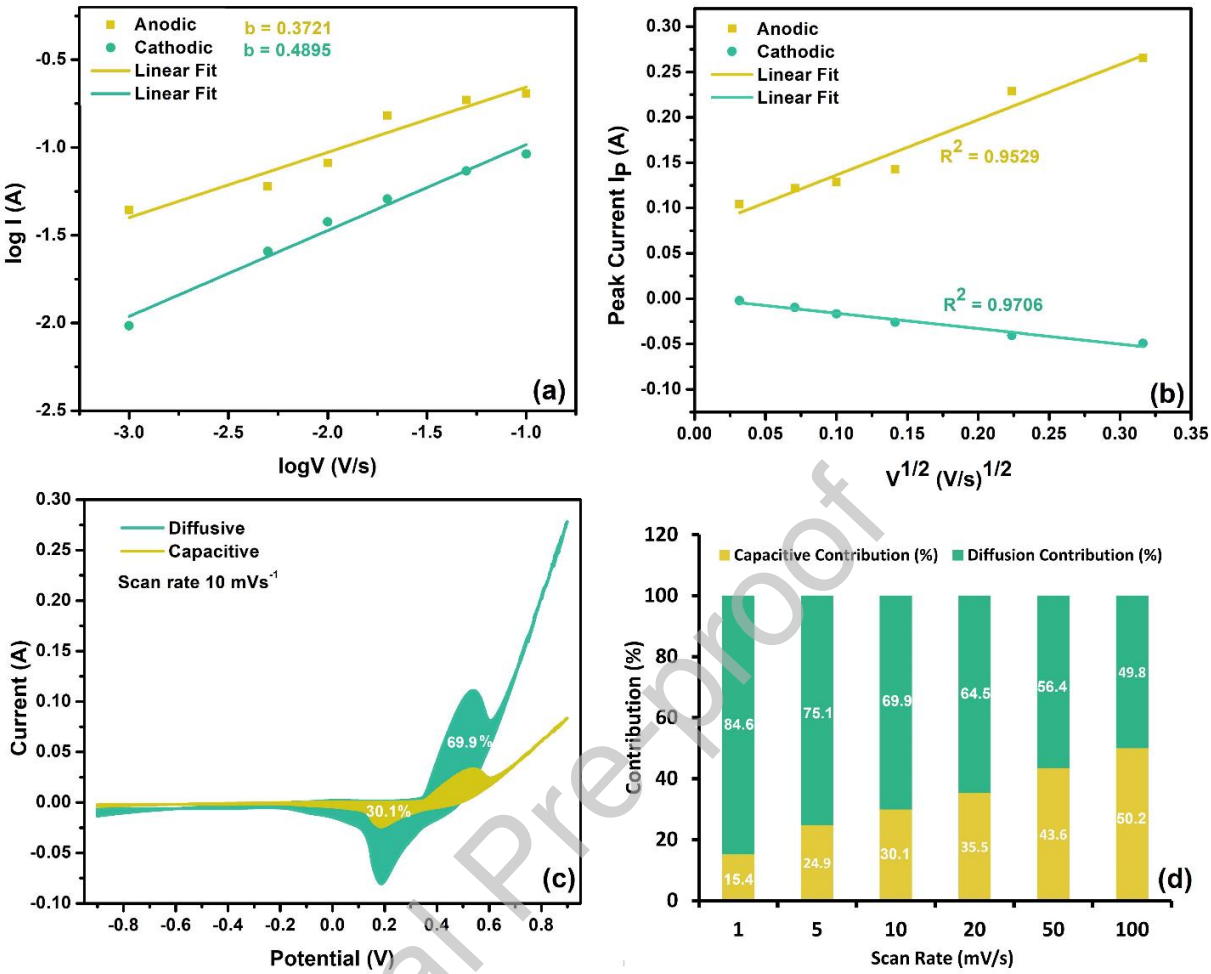

Figure 7: (a) logarithmic graph of current vs scan rate for the MGB 2 electrode, (b) current vs $v^{1/2}$ plot for anodic and cathodic peaks, (c) Dunn plot indicating contribution of capacitive-type and diffusion-type responses at 10 mVs^{-1}, (d) bar plot showing the capacitive and diffusion behavior at multiple sweep rates.

Table 1: C_{SP} values of MGB2 nanocomposite from CV analysis.

Scan rate (mVs^{-1})	**Specific Capacitance ($F\ g^{-1}$)**						
	MLG	**Biochar**	**MoO3**	**MoO3/MLG**	**MoO3/Biochar**	**MBG 1**	**MBG 2**
1	84.6	95.9	122.9	133.5	206.4	248.7	367.8
5	72.1	43.1	118.9	132.9	153.5	136.6	235.1
10	57.6	29.3	90.7	128.9	118.5	95.4	159.8

20	43.7	17.7	67.7	100.3	87.5	78.5	132.5
50	30.2	10.6	43.4	66.4	54.2	57.6	97.1
100	18.2	7.8	29.8	39.3	37.6	52.2	72.3

3.5 Galvanostatic Charging/Discharging (GCD)

The GCD analysis is performed to investigate the EC performance of the prepared nanocomposite as a supercapacitor electrode. The GCD graphs of MGB 2, MGB 1, MoO_3/Biochar, MoO_3/MLG, MoO_3, Biochar and MLG are depicted in Figure 8(a-g). The GCD profiles of composites show the pseudocapacitive response of the synthesized material due to the presence of non-linear behavior of the charging-discharging curves. MGB 2 has shown longer charging and discharging times as compared to the GCD curves of other materials. The C_{SP} for each electrode is estimated from the GCD profiles at multiple current densities. Figure 8(h) depicts the comparison of C_{SP} values of all synthesized composites at multiple current densities. At 1 Ag^{-1}, the estimated values of C_{SP} for MoO_3/MLG, MoO_3/biochar, MGB 1, and MGB 2 were 134, 151.9, 165.5, and 385 $Fg^{-1,}$ respectively. For comparison, C_{SP} of individual components were also calculated at different current densities. The C_{SP} values for biochar, MLG and MoO3 are calculated to be 65.7, 104.2, and 81.8F $g^{-1,}$ respectively. To further assess the rate capability of these composites at lower current densities, GCD measurements were also carried out for all three samples. At 0.2 Ag^{-1}, the corresponding C_{sp} values were increased to 180.8, 222.1, 240.2, and 472.6 F g^{-1} for MoO_3/MLG, MoO_3/Biochar, MGB 1, and MGB 2, respectively. The E_d and P_d of prepared nanocomposites were estimated at multiple current densities. For 1 Ag^{-1}, the E_d of MoO_3/Biochar, MGB 1, and MGB 2 were found to be 6.2, 6.9 and 16.17 Wh kg^{-1} while the corresponding values of P_d were 127.5, 312.5 and 305.5 W kg^{-1}. The enhanced charge storage behavior of MGB 2 can be credited to the combined effect of all three components of the composite which provide an optimum balance between ion accessibility, conductivity and electroactive surface area [64]. Furthermore, the ternary framework of MGB 2 has the advantage of having a well-tuned synergy between enhanced pseudocapacitance of MoO_3, the conductive foundation of graphitized carbon, and structural porosity of biochar. On the other hand, slight deviation of this fine-tuned composition in MGB 1 disturbs this balance, reducing the synergistic effect and in case of MoO_3/biochar, the absence of graphitized carbon further reduces the electrochemical performance of the composite. These findings emphasize that even a small

change in the ratio of components within the ternary architecture can have a huge effect on the EC properties of the nanocomposite. The overall comparison of different electrochemical parameters of all the samples at 1 A g^{-1} are given in Table 2.

Table 2: Comparison of C_{SP}, E_d, P_d values of all synthesized materials at 1 A g^{-1}.

Material	Specific capacitance ($F\ g^{-1}$)	Energy density ($Wh\ kg^{-1}$)	Power density ($W\ kg^{-1}$)
Multilayer Graphene	104.2	7.09	350
Biochar	65.7	9.12	500
MoO3	81.8	4.35	275
MoO3/Biochar	151.9	7.21	305.5
MoO3/MLG	134	4.65	250
MGB 1	165.57	6.95	312.5
MGB 2	385.06	16.17	305.5

3.6 EIS analysis

The EIS was utilized to examine the charge transportation characteristics of all prepared electrode materials. The Nyquist plots of MoO_3/biochar, MGB 1, and MGB 2 obtained between the frequency of 10 to 100 kHz are shown in figure 8(i). EIS curves of MGB 1 and MGB 2 have a depressed semicircle at elevated frequency part that is associated to the solution resistance (R_S) and the value of the diameter of the distorted semicircle determines the associated charge transfer resistance (R_{CT}) of the nanocomposites. The estimated value of R_S for MoO_3/biochar, MGB 1, and MGB 2 was 0.81, 0.77 and 0.63 Ω and the estimated R_{CT} were 4.81, 4.15, and 3.65 Ω, respectively. MGB 2 has lower value of R_{CT} as compared to MoO_3/biochar, MGB 1, this low value of R_{CT} suggests superior charge transportation at the electrode interfacial region for MGB 2. The linear part of the plot in the lower and intermediate frequency indicates the Warburg impedance which indicates highly efficient ions diffusion on the electrode surface. The EIS analysis confirms that MGB 2 has improved charge transport kinetics because of its lower internal resistance and enhanced ion/electron transport pathways [65]. Table 3 represents the specific capacitance comparison of MGB2 with literature.

Journal Pre-proof

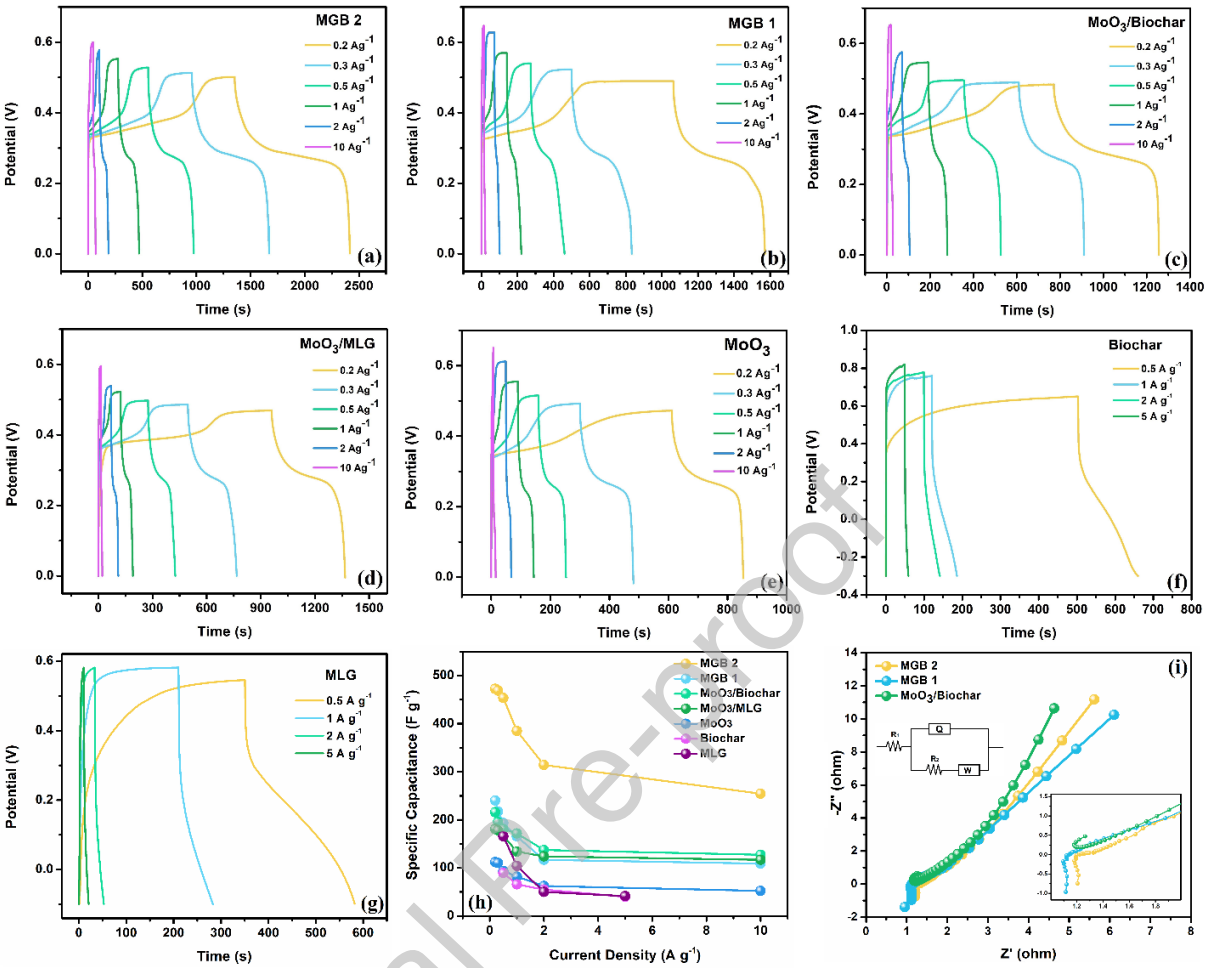

Figure 8: (a) GCD profile of MGB 2 at multiple current densities, (b) GCD profile of MGB 1, (c) GCD profile of MoO_3/Biochar, (d) GCD profile of MoO_3/MLG, (e) GCD profile of MoO_3, (f) GCD profile of Biochar, (g) GCD profile of MLG, (h) comparative plot of C_{SP} of all synthesized composites and individual components at various current densities, (i) Nyquist plots of MoO_3/Biochar, MGB 1, and MGB 2

Journal Pre-proof

Table 3: The comparative view of the specific capacitance of MGB 2 with previously reported literature.

Material	Electrolyte	Specific capacitance	Reference
MoO_3-rGO	1 M KOH	133.68 F g^{-1} (1 A g^{-1})	[8]
C-MoO_3-NiO_2/NF	6 M KOH	180.77 F g^{-1} (1 A $g^{-1)}$	[66]
gC_3N_4/MoO_3-GO	3 M KOH	468.9 C g-1 (0.5 A g-1)	[67]
MoS_2-NFs/f-WPB	6 M KOH	285 C g^{-1} (1 A g^{-1})	[68]
MXene/MoO_3	3 M H_2SO_4	418.2 C g^{-1} (0.5 A g^{-1})	[69]
MXene/rGO/MoO_3	1 M H_2SO_4	123.5 F g^{-1} (1 A g^{-1})	[70]
rGO/MoO_3@C	1 M H_2SO_4	562 F g^{-1} (1 A g^{-1})	[71]
h-MoO_3/GO	1 M H_2SO_4	134 Fg^{-1}(1 A g^{-1})	[72]
gC_3N_4/MoO_2/MoO_3	1 M KOH	151.1 C g^{-1} (0.2 A g^{-1})	[73]
MoO_3/rGO/CC	0.5 M Na_2SO_4	341.0 F g^{-1} (1 mV s^{-1})	[74]
CNF/MoO_3	2 M KOH	134.4 F g^{-1} (0.7 A g^{-1})	[75]
PEDOT-MoO_3@CNO	4.5 M H_2SO_4	348 F g^{-1}(1 A g^{-1})	[76]
Pd/MoO_3–rGO	6 M KOH	291.50 F g^{-1}(0.5 A g^{-1})	[77]
C/MoO_3	6 M KOH	115 F g^{-1}(0.5 A g^{-1})	[78]
Graphene-based MoO_3	1M Na_2SO_4	275 F g^{-1} (1 A g^{-1})	[79]
β-MoO_3@C	1 M KOH	80.7 F g^{-1} (0.2 A g^{-1})	[80]
h-MoO_3 doped graphene	2 M KOH	490.30 mF cm^{-1} (1 mA cm^{-1})	[81]
MoO3/MLG/Biochar (MGB 2)	**1M KOH**	**385 F g^{-1} (1 A g^{-1})** **367.8 F g^{-1} (1 mV s^{-1})**	**This work**

EC analysis of Asymmetric supercapacitor device

To understand the practical use of MGB 2, an asymmetric device was prepared with the ternary composite MGB 2 and activated carbon as active electrode materials. For the device fabrication, Ni-foam was utilized as a current collector, a permeable membrane was used as a separator between the two electrodes, and 2 M KOH was utilized as an electrolyte solution between the electrodes. The permeable membrane was dipped into the electrolyte and placed at the center of the electrodes. The schematic drawing of the prepared asymmetric cell is displayed in Figure 9(a), and the real fabricated device image is shown in Figure 9(b).The voltage range for the

prepared supercapacitor cell was optimized by doing CV measurements at 50 mVs^{-1} using different applied potentials. The electrochemical measurement of the prepared device was done using a two-electrode electrochemical cell system. The CV analysis was performed for a prepared supercapacitor cell at multiple scan rates from 5 mVs^{-1} to 100 mVs^{-1} with the potential range of -0.6 to 1.8 V at room temperature, shown in Figure 10(a). Obtained CV profiles of the MGB 2//AC device indicated broad and distinct redox humps, which can be associated with the faradic charge storage processes occurring at the surface of electrodes. These redox features show that the charge storage behavior of the device is dominantly pseudocapacitive in nature [82]. A gradual increase in the current response was analyzed in the CV profiles with an increase in the sweep rate. Although curves broaden slightly at high scan rates, the overall shape and redox peaks of the curves remain preserved. The retention of the peaks and curve symmetry at high sweep rates confirms the structural stability of the fabricated supercapacitor device [83].

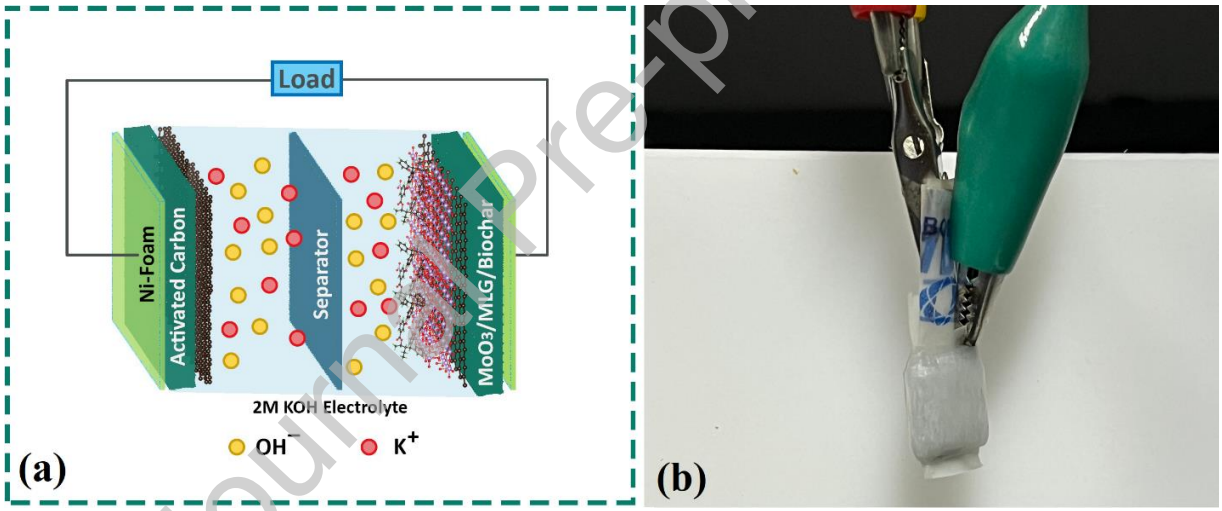

Figure 9: (a) Graphical illustration for MGB 2//AC asymmetric device, (b) Image of the prepared asymmetric supercapacitor device

GCD curves of the MGB 2//AC device are shown in Figure 10(b). The curves exhibit a quasi-triangular geometry with non-linear behavior, which confirms the pseudocapacitive behavior of the device. At 1 A g^{-1}, the device gave a longer charging-discharging time, indicating a high specific capacitance value [84]. The charging-discharging time decreased with an increase in the current density; this behavior can be associated with the limited ion diffusion into the bulk of the electrode surface at higher current densities [85]. The overall geometry of the curves remained

stable without significant distortion, showing good stability of the fabricated cell. The fabricated supercapacitor device achieved a highest C_{SP} of 132.8 F g^{-1} at 1 A g^{-1}. Even at 10 A g^{-1}, the device delivered C_{SP} of 79.09 F g^{-1}, indicating enhanced rate-capability. Figure 10(c) presents the variation of C_{SP} with current densities estimated from GCD analysis. For the MGB 2//AC device, the energy density (E_d) was estimated to be 46.65 Wh kg^{-1} with a power density (P_d) of 795 W kg^{-1} at 1 A g^{-1}. Figure 10(d) displays the Ragone plot, which shows the relationship of the achieved E_d and P_d of the fabricated MGB 2//AC cell. The obtained specific capacitance, E_d and P_d values are summarized in table 3.

Table 4: GCD results of the prepared MGB 2//AC device, showing C_{SP}, E_d, and P_d at multiple current densities.

Current Density (A g^{-1})	**Specific Capacitance (F g^{-1})**	**Energy density (Wh kg^{-1})**	**Power density (kW kg^{-1})**
1	132.8	46.65	0.79
2	121.7	45.46	1.6
4	111.3	44.18	3.3
6	101.1	42.03	5.1
8	96.5	40.58	6.9
10	79.0	34.41	8.8

The asymmetric device was subjected to the cyclic performance test for 7000 cycles at 10 A g^{-1}. Figure 10(e) shows the capacitance retention profile of the device. The device maintained 93.45% of its starting capacitance after 2000 cycles, 92.85% after 4500 cycles, and after 7000 cycles the device maintained 91.27% of its initial C_{SP}. These results confirmed the enhanced cyclic stability of the prepared device. The first and final 15 cycles of the cyclic stability test are presented in figure 10(inset:(e)). EIS analysis was carried out for the device between the frequency window of 0.01 to 100 kHz. Figure 10(f) shows the Nyquist plot of the MGB 2//AC device before and after 7000 cycles. A depressed semicircle was visible at the high-frequency part, whereas the low-frequency part exhibited a straight line. The solution resistance from the equivalent circuit was estimated to be 0.87 Ω. It was observed that the Rs value was decreased

slightly after 7000 cycles; these results indicate the enhanced charge transportation of the fabricated device [86]. The prepared nanocomposite demonstrated superior electrochemical performance along with excellent cyclic stability, confirming its suitability for supercapacitor applications.

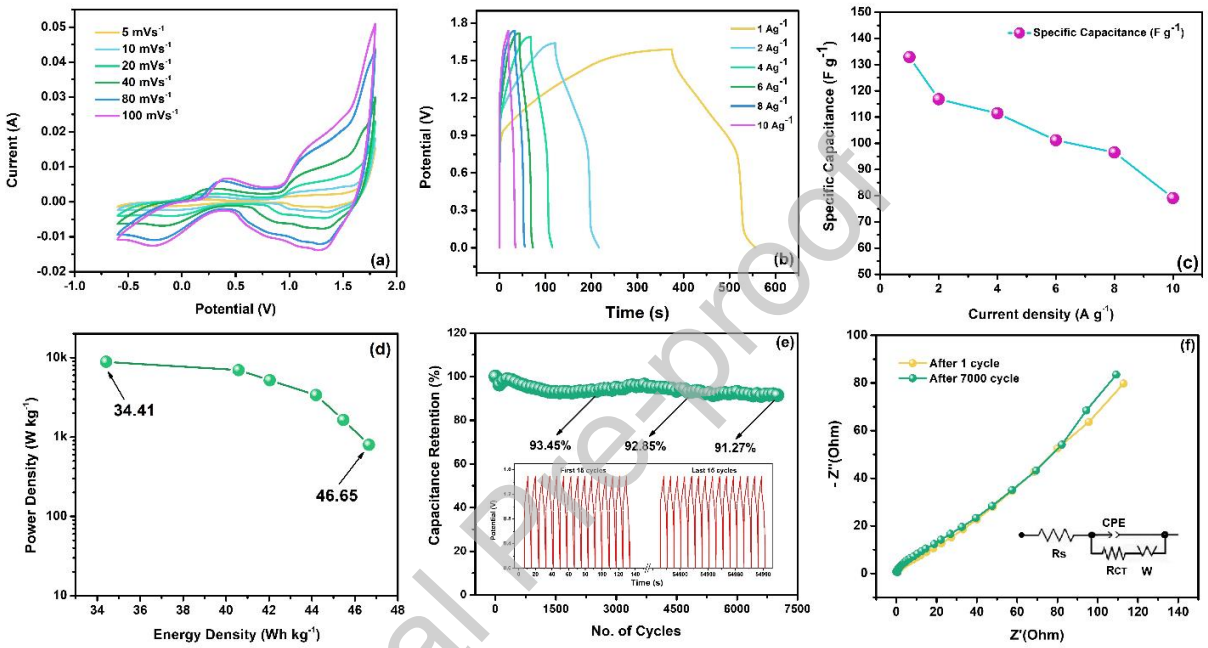

Figure 10: (a) CV profiles of the fabricated asymmetric device between 5 to 100 mV s^{-1} sweep rates, (b) GCD profiles of the device at 1 to 10 A g^{-1} current densities, (c) plot of achieved C_{SP} at multiple current densities from GCD measurements, (d) Ragone plot, (e) Cyclic stability plot, 15 first and last cycles (inset: (e)), (f) Nyquist plots for assembled asymmetric device before and after 7000 charging-discharging cycles

4 Conclusion

In this research, we successfully synthesized ternary nanocomposites of MoO_3, MLG, and activated biochar using a cost-effective and scalable hydrothermal method. The structural, morphological, and electrochemical measurements revealed that the ternary composite MGB 2 with an optimized composition of 80:10:10 (MoO_3:MLG:Biochar) exhibited enhanced performance. XRD results confirmed the successful formation of orthorhombic MoO_3 embedded

on MLG and biochar matrix. BET analysis confirmed the presence of a porous structure within the composite due to the integration of biochar. The FTIR and XPS analysis verified elemental composition and chemical states of the synthesized materials. SEM images further confirmed the successful integration of MoO_3, MLG, and activated biochar. TEM micrographs confirmed the integration of crystalline MoO3, graphene nanosheets and amorphous biochar in the MGB 2 nanocomposite. The ternary composite MGB 2 showed a specific capacitance of 385.06 F g^{-1} at 1 A g^{-1}, which outperformed MoO_3/MLG, MoO_3/Biochar, and MGB 1 composite. EIS measurements demonstrated enhanced charge transport kinetics of the composite. Furthermore, the Dunn plot and power law analysis demonstrated a diffusion-type charge storage mechanism, which is suitable for longer energy storage. The fabricated asymmetric supercapacitor device delivered C_{SP} of 132.8 F g^{-1} with a maximum energy density of 46.65 Wh kg^{-1} and a power density of 795 W kg^{-1} at 1 A g^{-1}. The device delivered 91.27% of capacitance retention after 7000 cycles.This work not only introduced a promising electrode architecture for efficient supercapacitors but also emphasized using biomass-based carbon with transition metal oxides and graphitic materials for sustainable energy storage applications.

Acknowledgement

This work has been done with the support of Pakistan Council of Scientific & Industrial Research (PCSIR). The authors gratefully acknowledge PCSIR for its valuable assistance.

Journal Pre-proof

References

1. Lu, W., Si, Y., Zhao, C., Chen, T., Li, C., Zhang, C., & Wang, K. (2024). Biomass-derived carbon applications in the field of supercapacitors: Progress and prospects. *Chemical Engineering Journal*, *495*, 153311.

2. Yan, J., Lu, J., Sheng, Y., Sun, Y., & Zhang, D. (2024). Research progress in the preparation of transition metal sulfide materials and their supercapacitor performance. *Micromachines*, *15*(7), 849.
3. Muduli, S., Pani, T. K., Garlapati, K. K., & Martha, S. K. (2024). Carbon nano-onions triggering the supercapacitive performance of PEDOT-wrapped MoO_3 microstructures in hybrid ultracapacitors. Journal of Energy Storage, 95, 112396.
4. Dalvand, S., Foroozandeh, A., Heydarian, A., Nasab, F. S., Omidvar, M., Yazdanfar, N., & Asghari, A. (2024). A review on carbon material-metal oxide-conducting polymer and ionic liquid as electrode materials for energy storage in supercapacitors. *Ionics*, *30*(4), 1857-1870.
5. Sethi, M., Shenoy, U. S., & Bhat, D. K. (2021). Simple solvothermal synthesis of porous graphene-NiO nanocomposites with high cyclic stability for supercapacitor application. *Journal of Alloys and Compounds*, *854*, 157190.
6. Sethi, M., Shenoy, U. S., & Bhat, D. K. (2024). Iron Oxide-Functionalized Graphene Nanocomposites for Supercapacitor Application. In *Iron Oxide-Based Nanocomposites and Nanoenzymes: Fundamentals and Applications* (pp. 77-117). Cham: Springer International Publishing.
7. Sethi, M., & Bhat, D. K. (2019). Facile solvothermal synthesis and high supercapacitor performance of NiCo2O4 nanorods. *Journal of Alloys and Compounds*, *781*, 1013-1020.
8. Reddy, B. J., Vickraman, P., & Justin, A. S. (2019). Microwave synthesis of MoO_3-reduced graphene oxide nanocomposite for high performance asymmetric supercapacitors. *Journal of Materials Science: Materials in Electronics*, *30*, 3618-3628.
9. Dilwale, G. V., Piao, G., Kim, H., Pawar, A. C., Said, Z., Nimat, R. K., ... &Bulakhe, R. N. (2024). Chemical route synthesis of nanohybrid MoO_3-rGO for high-performance hybrid supercapacitors. *Journal of Energy Storage*, *91*, 112050.
10. Rogier, C., Pognon, G., Galindo, C., Nguyen, G. T. M., Vancaeyzeele, C., & Aubert, P. H. (2022). MoO_3–carbon nanotube negative electrode designed for a fully hybrid asymmetric metal oxide-based pseudocapacitor operating in an organic electrolyte. *ACS Applied Energy Materials*, *5*(8), 9361-9372.
11. Awadallah, A. E., Aboul-Enein, A. A., Yousif, N. M., Azab, M. A., & Haggar, A. M. (2025). Plastic Waste-Derived Carbon Nanotubes Decorated with Mo2C, MoO_3, or MoO_3/Mo_2C as

Journal Pre-proof

Effective Nanocomposite Materials for Supercapacitor Applications. *ChemistrySelect*, *10*(17), e202500750.

12. Bhat, D. K., Bantawal, H., Uma, P. I., Kumar, S. P., & Shenoy, U. S. (2024). Designing sustainable porous graphene-CaTiO3 nanocomposite for environmental remediation. *Sustainable Chemistry for the Environment*, *5*, 100071.
13. Bhat, D. K., Bantawal, H., & Shenoy, U. S. (2023). Enhanced photoresponse and efficient charge transfer in porous graphene-BaTiO3 nanocomposite for high performance photocatalysis. *Diamond and Related Materials*, *139*, 110312.
14. Mamani, A., Barreda, D., Sardella, M. F., Bavio, M., Blanco, C., González, Z., & Santamaría, R. (2024). Fe-doped biomass-derived activated carbons as sustainable electrode materials in supercapacitors using different electrolytes. *Journal of Electroanalytical Chemistry*, *965*, 118366.
15. Zhu, X., Zeng, Y., Zhao, X., Liu, D., Lei, W., & Lu, S. (2025). Biomass-Derived Carbon and Their Composites for Supercapacitor Applications: Sources, Functions, and Mechanisms. *EcoEnergy*, e70000.
16. Khedulkar, A. P., Yu, W. J., Pandit, B., & Doong, R. A. (2024). Boosting supercapacitor performance with a cobalt hydroxide in-situ preparation orange peel biochar flower-like composite. *Journal of Energy Storage*, *81*, 110302.
17. Xiao, J., Yuan, X., Li, W., Zhang, T. C., He, G., & Yuan, S. (2024). Cellulose-based aerogel derived N, B-co-doped porous biochar for high-performance CO2 capture and supercapacitor. *International Journal of Biological Macromolecules*, *269*, 132078.
18. Talha, M., Akram, R., Akhtar, H., Karamat, S., Kanwal, S., & Sabir, I. (2025). Enhanced Electrochemical Behavior of Ni-doped MoO3 and Reduced Graphene Oxide Composite for Lithium-ion Batteries. Results in Engineering, 106705.
19. Liu, M., Wang, L., & Yu, G. (2024). Recent research progress of porous graphene and applications in molecular sieve, sensor, and supercapacitor. *Small*, *20*(42), 2401767.
20. Makinde, W. O., Hassan, M. A., Pan, Y., Guan, G., Lopez-Salas, N., & Khalil, A. S. (2024). Sulfur and nitrogen co-doping of peanut shell-derived biochar for sustainable supercapacitor applications. *Journal of Alloys and Compounds*, *991*, 174452.
21. Liu, Y., Zhang, B. H., Xiao, S. Y., Liu, L. L., Wen, Z. B., & Wu, Y. P. (2014). A nanocomposite of MoO_3 coated with PPy as an anode material for aqueous sodium

Journal Pre-proof

rechargeable batteries with excellent electrochemical performance. *Electrochimica acta*, *116*, 512-517.

22. Avani, A. V., Chrisma, R. B., & Anila, E. I. (2023). Low temperature synthesis of MoO_3 nanoparticles by hydrothermal method: Investigation on their structural and optical properties. *Materials Today: Proceedings*, *80*, 629-633.
23. Zhu, H., Xu, J., Zhang, P., Chen, J. P., & Shao, L. (2025). Elemental precursor strategy for anchoring hierarchical NiS/Ni3S2 heterostructures on multi-layer graphene for high-performance supercapacitors. *Electrochimica Acta*, 146625.
24. Hariyanto, B., Wardani, D. A. P., Kurniawati, N., Har, N. P., & Darmawan, N. (2021, October). X-ray peak profile analysis of silica by Williamson–Hall and size-strain plot methods. In *Journal of Physics: Conference Series* (Vol. 2019, No. 1, p. 012106). IOP Publishing.
25. Medeiros Leão, G. S., Silva Ribeiro, M. D., Filho, R. L. D. F., Saraiva, L. B., Peña-Garcia, R. R., Teixeira, A. P. D. C., ... & Nobre, F. X. (2024). The synergic effect of h-MoO3, α-MoO3, and β-MoO3 phase mixture as a solid catalyst to obtain methyl oleate. *ACS Applied Materials & Interfaces*, *16*(44), 60103-60121.
26. Al-Muntaser, A. A., Althobiti, R. A., Morsi, M. A., Alsalmah, H. A., Tarabiah, A. E., Alzahrani, E., ... & Abdallah, E. M. (2024). MoO3 nanoplates reinforced the structural, electrical, mechanical, and antibacterial characteristics of polyvinyl pyrrolidone/sodium alginate polymer blend for optoelectronics and biological applications. *International Journal of Biological Macromolecules*, *254*, 127894.
27. Khiar, H., Janani, F. Z., Sadiq, M. H., Qourzal, S., Puga, A., & Barka, N. (2025). MoO3 decorated Ag3PO4: nn heterojunction for high photocatalytic performance and improved stability. *Materials Research Bulletin*, *184*, 113253.
28. Ebrahimi Naghani, M., Neghabi, M., Zadsar, M., &Abbastabar Ahangar, H. (2023). Synthesis and characterization of linear/nonlinear optical properties of graphene oxide and reduced graphene oxide-based zinc oxide nanocomposite. *Scientific Reports*, *13*(1), 1496.
29. Misra, A., Tyagi, P. K., Singh, M. K., & Misra, D. S. (2006). FTIR studies of nitrogen doped carbon nanotubes. *Diamond and related materials*, *15*(2-3), 385-388.
30. Karthik, V., Mohanasundaram, S., Ramaraju, P., Jeyanthi, J., & Periyasamy, S. (2023). Study on the production, characterization, and application of coconut fiber biochar for effective

Journal Pre-proof

removal of Co (II) ions from synthetic wastewater. *Biomass Conversion and Biorefinery*, *13*(15), 13677-13693.

31. Wang, B. B., Zhong, X. X., Ming, B. M., Zhu, M. K., Chen, Y. A., Cvelbar, U., & Ostrikov, K. (2019). Structure and photoluminescence properties of MoO3− x/graphene nanoflake hybrid nanomaterials formed via surface growth. *Applied Surface Science*, *480*, 1054-1062.
32. Raj, A. N. P., Bennie, R. B., Joel, C., Kengaram, S. H., & Abraham, S. D. (2022). Systematic analysis and the effect of Mn doping on structural, optical and magnetic properties of MoO_3 nanoparticles. *Solid State Communications*, *341*, 114532.
33. Fan, Z., Zhang, X., Zhou, M., Yang, Y., & Wen, G. (2023). High sensitivity ethanol sensor based on MoO_3 nanoparticles and its sensing mechanism. *Journal of Materials Science: Materials in Electronics*, *34*(4), 275.
34. Kalantar-Zadeh, K., Tang, J., Wang, M., Wang, K. L., Shailos, A., Galatsis, K., ... & Kaner, R. B. (2010). Synthesis of nanometre-thick MoO 3 sheets. *Nanoscale*, *2*(3), 429-433.
35. Almodóvar, P., Díaz-Guerra, C., Ramírez-Castellanos, J., & González-Calbet, J. M. (2018). In situ local assessment of laser irradiation-induced phase transformations in hexagonal MoO 3 microrods. *CrystEngComm*, *20*(34), 4954-4961.
36. Sethi, M., Bantawal, H., Shenoy, U. S., & Bhat, D. K. (2019). Eco-friendly synthesis of porous graphene and its utilization as high performance supercapacitor electrode material. *Journal of Alloys and Compounds*, *799*, 256-266.
37. Tang, R., Gong, D., Deng, Y., Xiong, S., Zheng, J., Li, L., ... & Zhao, J. (2022). π-π stacking derived from graphene-like biochar/g-C3N4 with tunable band structure for photocatalytic antibiotics degradation via peroxymonosulfate activation. *Journal of Hazardous Materials*, *423*, 126944.
38. Xu, J., Tang, M., Hu, Z., Hu, X., Zhou, T., Song, K., ... & Cheng, J. (2021). Standing and lying Ni (OH) 2 nanosheets on multilayer graphene for high-performance supercapacitors. *Nanomaterials*, *11*(7), 1662.
39. Su, J. Z., Wang, C. C., Zhang, M. Y., Zong, X. B., Huang, X. F., Deng, Z. H., & Xiang, P. (2023). Advances and prospectives of iron/biochar composites: Application, influencing factors and characterization methods. *Industrial Crops and Products*, *205*, 117496.
40. Thommes, M., Kaneko, K., Neimark, A. V., Olivier, J. P., Rodriguez-Reinoso, F., Rouquerol, J., & Sing, K. S. (2015). Physisorption of gases, with special reference to the evaluation of

Journal Pre-proof

surface area and pore size distribution (IUPAC Technical Report). *Pure and applied chemistry*, *87*(9-10), 1051-1069.

41. Kundu, M., Mondal, D., Mondal, I., Baral, A., Halder, P., Biswas, S., ... & Das, S. (2023). A rational preparation strategy of phase tuned MoO3 nanostructures for high-performance all-solid asymmetric supercapacitor. *Journal of Energy Chemistry*, *87*, 192-206.
42. Nyholm, R., & Martensson, N. (1980). Core level binding energies for the elements Zr-Te (Z= 40-52). *Journal of Physics C: Solid State Physics*, *13*(11), L279.
43. Wu, C., Liu, D., Li, H., & Li, J. (2018). Molybdenum carbide-decorated metallic cobalt@ nitrogen-doped carbon polyhedrons for enhanced electrocatalytic hydrogen evolution. *Small*, *14*(16), 1704227.
44. Kuznetsov, M. V., Volkov, V. L., Zhakharova, G. S., & Gubanov, V. A. (1994). XPS study of catalytic compounds H2V12− xMexO31− δ nH2O (Me: Mo, Cr). *Journal of electron spectroscopy and related phenomena*, *68*, 579-588.
45. Jahan, F., & Smith, B. E. (1992). Investigation of solar selective and microstructural properties of molybdenum black immersion coatings on cobalt substrates. *Journal of materials science*, *27*(3), 625-636.
46. Al-Shihry, S. S., &Halawy, S. A. (1996). Unsupported MoO3□ Fe2O3 catalysts: characterization and activity during 2-propanol decomposition. *Journal of Molecular Catalysis A: Chemical*, *113*(3), 479-487.
47. Kim, K. S., Baitinger, W. E., Amy, J. W., & Winograd, N. (1974). ESCA studies of metal-oxygen surfaces using argon and oxygen ion-bombardment. *Journal of electron spectroscopy and related phenomena*, *5*(1), 351-367.
48. Patterson, T. A., Carver, J. C., Leyden, D. E., & Hercules, D. M. (1976). A surface study of cobalt-molybdena-alumina catalysts using x-ray photoelectron spectroscopy. *The Journal of Physical Chemistry*, *80*(15), 1700-1708.
49. Lima, C. D., de Carvalho, T. C., Mendoza, C. D., da Costa, M. E. M., Pinheiro, G. D. S., Luz-Lima, C., ... & Araujo, J. F. (2025). Magnetic transition in MoO3: Influence of Mo5+/Mo6+ ratios on paramagnetic to diamagnetic behavior. *Solid State Sciences*, *162*, 107866.
50. Powell, C. J. (2012). Recommended Auger parameters for 42 elemental solids. *Journal of Electron Spectroscopy and Related Phenomena*, *185*(1-2), 1-3.

51. Thangappan, R., Arivanandhan, M., Kalaiselvam, S., Jayavel, R., & Hayakawa, Y. (2018). Molybdenum oxide/graphene nanocomposite electrodes with enhanced capacitive performance for supercapacitor applications. *Journal of Inorganic and Organometallic Polymers and Materials*, *28*(1), 50-62.
52. Wu, W., Shuai, M., Kuang, H., Zhang, H., Zhang, W., Chen, H., & Ling, Q. (2021). Synthesis of NiCo-layered double hydroxide/multilayer graphene composite via the ozone oxidation combined microwave-assisted synthesis strategy. *Diamond and Related Materials*, *120*, 108636.
53. Sahoo, P. K., Kumar, N., Jena, A., Mishra, S., Lee, C. P., Lee, S. Y., & Park, S. J. (2024). Recent progress in graphene and its derived hybrid materials for high-performance supercapacitor electrode applications. *RSC advances*, *14*(2), 1284-1303.
54. Husain, Z., Raheman, A. S., Ansari, K. B., Pandit, A. B., Khan, M. S., Qyyum, M. A., & Lam, S. S. (2022). Nano-sized mesoporous biochar derived from biomass pyrolysis as electrochemical energy storage supercapacitor. *Materials Science for Energy Technologies*, *5*, 99-109.
55. Amba Sankar, K. N., Kesavan, L., Saha, B., Jyolsnaraj, M. K., Mohan, S., Nandakumar, P., ... &Kvarnström, C. (2024). Renewable synthesis of MoO3 nanosheets via low temperature phase transition for supercapacitor application. *Scientific Reports*, *14*(1), 20503.
56. Lee, H. J., Shim, H. W., Kim, J. C., & Kim, D. W. (2017). Mo-MoO3-graphene nanocomposites as anode materials for lithium-ion batteries: scalable, facile preparation and characterization. *Electrochimica Acta*, *251*, 81-90.
57. Wang, X., Liu, K., Li, J., Liu, Y., Wang, M., & Cui, H. (2023). Creation of an extrinsic pseudocapacitive material presenting extraordinary cycling-life with the battery-type material Co (OH) 2 by S2− doping for application in supercapacitors. *Chemical Engineering Journal*, *451*, 138969.
58. Jia, H., Wang, M., Feng, M., Li, G., Li, L., & Liu, Y. (2024). Synergistic enhancement of supercapacitor performance: Modish designation of BPQD modified NiCo-LDH/NiCo2S4 hybrid nanotube arrays with improved conductivity and OH–adsorption. *Chemical Engineering Journal*, *484*, 149591.

Journal Pre-proof

59. Saha, S., Routray, K. L., & Parida, A. (2025). Graphene-integrated Ag-doped $NiFe_2O_4$ nanostructures for high-performance supercapacitor application. *Diamond and Related Materials*, *155*, 112264.
60. Roy, P., Zubair, M. A., & Islam, M. R. (2025). Tuning the electrochemical performance of hierarchical MoO_3/CdO binary heterostructure for supercapacitor applications. *Nanoscale Advances*.
61. Marwat, M. A., Ishfaq, S., Adam, K. M., Tahir, B., Shaikh, M. H., Khan, M. F., ... & Ghazanfar, E. (2024). Enhancing supercapacitor performance of Ni–Co–Mn metal–organic frameworks by compositing it with polyaniline and reduced graphene oxide. *RSC advances*, *14*(3), 2102-2115.
62. Palani, H., & Rastogi, A. (2024). Effect of annealing temperature on structural and electrochemical behaviour on MgFe2O4 as electrode material in neutral aqueous electrolyte for supercapacitors. *Nanotechnology*, *35*(17), 175401.
63. Yan, C., Yang, X., Lu, S., Han, E., Chen, G., Zhang, Z., ... & He, Y. (2022). Hydrothermal synthesis of vanadium doped nickel sulfide nanoflower for high-performance supercapacitor. *Journal of Alloys and Compounds*, *928*, 167189.
64. Sundaresan, S., Subramanian, D., & Raju, G. (2023). Exploration of two dimensional MoO_3-Fe_2O_3 nanocomposite for the fabrication of high energy density supercapacitor applications. *Inorganic Chemistry Communications*, *148*, 110360.
65. Liu, C., Zhang, N., Huang, X., Wang, Q., Wang, X., & Wang, S. (2021). Fabrication of a novel nanocomposite electrode with ZnO-MoO3 and biochar derived from mushroom biomaterials for the detection of acetaminophen in the presence of DA. *Microchemical Journal*, *161*, *105719.*
66. Jin, Z., Hu, K., Lin, F., Liu, S., Gu, R., Zhang, W., ... & Ma, H. (2025). Nickel foam supported biochar doped Ni–Mo bimetallic oxide for supercapacitor application. *Reaction Chemistry & Engineering*, *10*(1), 224-236.
67. Ferozgandhi, K., Girirajan, M., Subramaniyan, S., Sangaraju, S., Ali, M., Raju, R., ... &Sakkarapani, S. (2025). Graphitic carbon nitride quantum dot embedded with MoO3-GO nanosheets as electrode material for enhanced supercapacitor performance. *Journal of Energy Storage*, *113*, 115743.

Journal Pre-proof

68. El-Sabban, H. A., Attia, S. Y., Mostafa, H. Y., & Mohamed, S. G. (2024). Rational design of MoS2 nanoflowers grafted highly porous functionalized woody pulp-derived biochar for sustainable energy storage devices. *Fuel*, *359*, 130485.
69. Ran, F., Tan, B., Hu, M., Deng, S., Wang, K., Sun, W., ... & Yang, X. (2025). Electrostatic self-assembly assisted construction of MXene/MoO3 hybrid aerogel for free-standing supercapacitor electrodes. *Chemical Engineering Journal*, *511*, 161851.
70. Li, R., Chen, L., Song, S., Zheng, B., Li, T., Zheng, W., & Ma, Y. (2025). Fabrication of MXene/reduced graphene oxide/MoO3 film electrode for flexible supercapacitors. *Journal of Energy Storage*, *131*, 117669.
71. Shaheen, W., Warsi, M. F., Shahid, M., Khan, M. A., Asghar, M., Ali, Z., ... & Shakir, I. (2016). Carbon coated MoO3 nanowires/graphene oxide ternary nanocomposite for high-performance supercapacitors. *Electrochimica Acta*, *219*, 330-338.
72. Kumbhar, A. A., Bachankar, S. S., Mullani, S. B., Lokhande, V. C., Kim, C., & Ji, T. (2024). Hydrothermal Synthesis and Electrochemical Characterizations of h-MoO3/Graphene Oxide for Enhanced Supercapacitive Performance. *Korean Journal of Materials Research*, *34*(11), 568-576.
73. Wang, T., Mallikarjuna, K., Vattikuti, S. P., Altaf, M., Goud, B. S., Koyyada, G., & Shim, J. (2024). Synergistic enhancement of electrochemical storage using g-C3N4 modified MoO2/MoO3 nanostructure electrodes via thermal decomposition. *Journal of Energy Storage*, *96*, 112716.
74. Li, S., & Li, Z. (2024). Flexible asymmetric supercapacitors constructed by reduced graphene oxide/MoO3 and MnO2 electrochemically deposited on carbon cloth. *Molecules*, *29*(13), 3116.
75. Chaji, A., Sajjadi, S. A., &Darband, G. B. (2024). Electrochemical efficiency of carbon nanofiber/molybdenum oxide nanocomposites synthesized by electrospinning used in supercapacitors and oxygen evolution reaction. *Journal of Electroanalytical Chemistry*, *965*, 118368.
76. Muduli, S., Pani, T. K., Garlapati, K. K., & Martha, S. K. (2024). Carbon nano-onions triggering the supercapacitive performance of PEDOT-wrapped MoO3 microstructures in hybrid ultracapacitors. *Journal of Energy Storage*, *95*, 112396.

Journal Pre-proof

77. Wanchan, W., Yogesh, G. K., Yeetsorn, R., Maiket, Y., &Koinkar, P. (2025). Synthesis and characterization of synergetic Pd/MoO3–rGO hybrid material as efficient electrode for supercapacitor application. *Materials Chemistry and Physics*, *331*, 130134.
78. Li, Q., Zhang, Y. F., Han, X. R., Ju, C., & Wang, Z. L. (2021). A comparison of MoO3 nanorods and C/MoO3 nanocomposites for high-performance supercapacitor electrode. *Chalcogenide Lett*, *18*(7), 413-420.
79. Cheng, A., Shen, Y., Hong, T., Zhan, R., Chen, E., Chen, Z., ... & Deng, S. (2022). Self-assembly vertical graphene-base MoO3 nanosheets for high performance supercapacitors. *Nanomaterials*, *12*(12), 2057.
80. Liu, X., Wu, Y., Wang, H., Wang, Y., Huang, C., Liu, L., & Wang, Z. (2020). Two-dimensional β-MoO 3@ C nanosheets as high-performance negative materials for supercapacitors with excellent cycling stability. *RSC advances*, *10*(30), 17497-17505.
81. Verma, V., Singh, R. S., Gupta, M., & Singh, A. K. (2025). Fermi-level tuning in graphene via green synthesized h-MoO3: Enhanced supercapacitor performance of h-MoO3 doped graphene. *Journal of Alloys and Compounds*, *1018*, 179225.
82. Faisal, M. M., Ali, S. R., Iqbal, M. Z., Iqbal, M. W., Numan, A., & Sanal, K. C. (2021). Effect of polyaniline on the performance of zinc phosphate as a battery-grade material for supercapattery. *Journal of Energy Storage*, *44*, 103329.
83. Sabir, I., Mingxia, H., Anwar, H., Kashif, M., &Yizhu, Z. (2025). Utilization of copper-doped zinc spinel ferrites nano-composites as battery-grade electrode materials for supercapattery device applications. *Journal of Energy Storage*, *112*, 115498.
84. Alam, A., Saeed, G., Mahmoudi, H., Shakya, J., & Tadesse, B. (2025). All MXene in-situ interfaced 0D/2D hybrid nanomaterials: 3D DIW printed asymmetric supercapacitor using binary Cu-Ni-O-FPs/MXene and a-Fe-O-FPs/MXene electrodes. *Results in Engineering*, 107167.
85. Sabir, I., Mingxia, H., Anwar, H., Masud, M. I., Aman, M., & Kashif, M. (2025). Synthesis and Investigation of Zinc-based Ca-doped ferrites composite for high-performance energy storage hybrid devices. *Results in Engineering*, 107411.
86. Mohanasundari, M., Elango, M., SP, L. S., Mohammad, S., Elayappan, V., Sangaraju, S., & Prabha, D. (2025). Pristine Ni-Sn layered-double-hydroxide and NiO/SnO_2 hierarchical

nanocomposites as high-performance electrode materials for supercapacitor applications. *Results in Engineering*, *27*, 105772.

87. Lakshmi-Narayana, A., Attarzadeh, N., Shutthanandan, V., & Ramana, C. V. (2024). High-performance NiCo2O4/graphene quantum dots for asymmetric and symmetric supercapacitors with enhanced energy efficiency. *Advanced Functional Materials*, *34*(40), 2316379.
88. Brundle, C. R., & Crist, B. V. (2020). X-ray photoelectron spectroscopy: A perspective on quantitation accuracy for composition analysis of homogeneous materials. *Journal of Vacuum Science & Technology A*, *38*(4).

Declaration of interests

☒ The authors declare that they have no known competing financial interests or personal relationships that could have appeared to influence the work reported in this paper.

☐ The authors declare the following financial interests/personal relationships which may be considered as potential competing interests:

Journal Pre-proof